



Modeling of the effects of weakness planes in rock masses on the stability of tunnels using an equivalent continuum and damage model

Guowen Xu¹ · Marte Gutierrez¹ · Chuan He² · Shimin Wang²

Received: 13 May 2020 / Accepted: 22 September 2020 / Published online: 6 February 2021

© This is a U.S. Government work and not under copyright protection in the US; foreign copyright protection may apply [2020] 2021

Abstract

This paper proposes an equivalent continuum model to describe the mechanical behavior of transversely isotropic rocks. In this model, the transverse isotropy of deformation and strength was achieved based on the Mohr–Coulomb and maximum tensile-stress criteria, and the damage was captured by adopting a statistical damage evolution rule. The application of the model is verified through numerical simulation of conventional triaxial tests. The model is then used to reveal the non-uniform mechanical response of the surrounding rock and the secondary lining for a tunnel situated in a weak layered rock mass. The results show that: (1) The proposed model can capture the transverse isotropy in deformation and strength of rocks, and the proposed damage formulation can represent the deterioration and degree of failure of rocks; (2) The fracturing pattern, failure strength and stress–strain curves obtained from the proposed model agree well with test results for three typical rocks with different directional variations in strength; (3) The damage distribution based on the proposed model can identify the failure of layered rock mass; and (4) The damage zones of the surrounding rock and the loads on the secondary lining after tunnel excavation show distinctly asymmetric behavior, that is, the damaged zones are concentrated in the tunnel direction normal to the weak planes, and the positive bending moment and larger axial force are parallel and vertical to the weak planes, respectively.

Keywords Damage mechanics · Elastoplasticity · Secondary lining · Transverse isotropy · Tunnel

1 Introduction

Layered structures due to bedding plane, foliation, stratification and fissuring bring directional anisotropy in the physical and mechanical behaviors of transversely isotropic rocks [29, 44]. In turn, anisotropy affects the failure patterns of rocks in almost all major engineering projects involving foundations, slopes or underground excavations [2, 17, 33, 57]. Thus, it is of vital importance to evaluate the mechanical behavior of transversely isotropic rocks.

Numerous compression tests have been conducted to study the strength anisotropy for transversely isotropic rocks, including sedimentary rocks, such as sandstone [14, 37, 58], limestone [12, 47], Marl [12], Coal [12], mudstone [43] and argillite [45]; metamorphic rocks, such as shale [3–6, 12, 21, 22, 27, 35, 47], phyllite [8, 30, 42, 53], slate [10, 20, 30, 47], schist [1, 18, 34] and gneiss [5]; igneous rocks, such as orthoquartzite [30]; and synthetic rocks [56].

Typically, strength anisotropy of transversely isotropic rocks shows three distinct features (Fig. 1): (1) the directional variations in strength can be classified into “U” type, “shoulder” type or “wavy” undulatory type, and the “U” type is the most common one among the three types [41] (Fig. 1a); (2) The maximum strength occurs at $\theta = 0^\circ$ or 90° and mostly at $\theta = 90^\circ$, where θ is the angle between the main loading direction and the orientation of the weak planes. The minimum strength appears at $\theta = 30^\circ$ – 45° ; and (3) The degree of anisotropy (the ratio between maximum

✉ Marte Gutierrez
mgutierr@mines.edu

¹ Department of Civil and Environmental Engineering, Colorado School of Mines, Golden, CO 80401, USA

² Key Laboratory of Transportation Tunnel Engineering, Ministry of Education, Southwest Jiaotong University, Chengdu 610031, Si Chuan, China

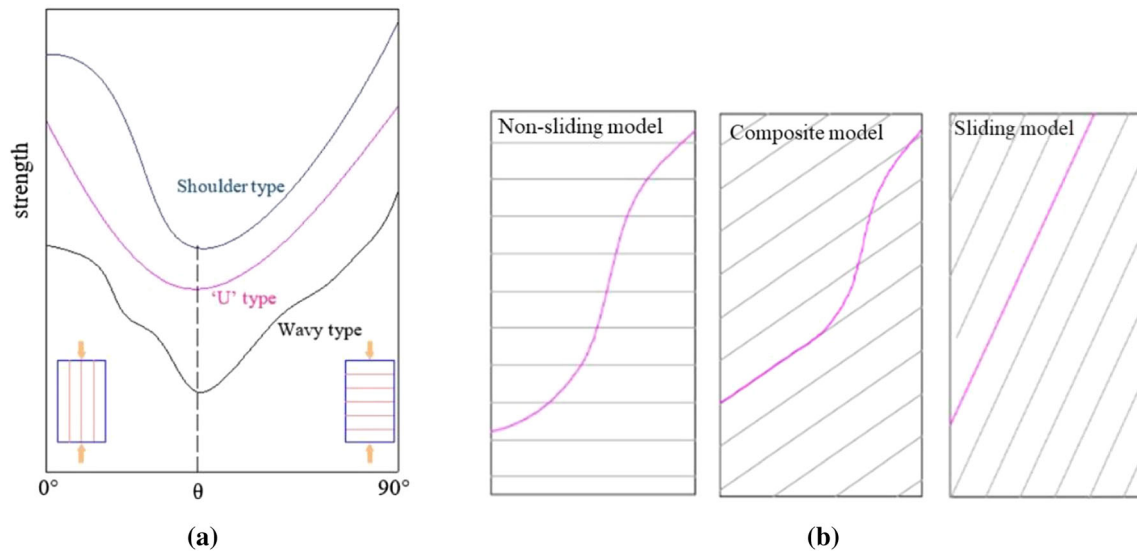


Fig. 1 Mechanical behavior of transversely isotropic rocks: **a** three different types of the directional variations of strength (Ramamurthy [41]); **b** failure patterns for transversely isotropic rocks

and minimum strength) decreases as the confining pressure increases in most cases and the strength types may change due to the confining effect. As for fracturing, the pattern changes according to the direction of loading with respect to the orientation of the weakness planes (Fig. 1b): (1) failure propagates through the rock matrix, i.e., the non-sliding model; (2) across and along weak planes, i.e., the composite model; and (3) along the weak planes, i.e., the sliding model. The non-sliding model becomes more dominant with the increase in the confining pressure.

In numerical simulations, the representation of the layered structures in the rock mass can be made implicitly (i.e., continuum-based methods [39, 40]) or explicitly (i.e., discontinuum-based methods). The commonly used discontinuous approaches are block or particle discrete element method (DEM) and discontinuous deformation analysis (DDA) method. In these techniques, the geometry and the behavior of the weak planes can be described explicitly. Thus, they are suitable to be adopted to study the anisotropic mechanisms of rocks from a mesoscopic view, such as the initiation, propagation and coalescence of cracks. For example, based on the Particle Flow Code [24, 50], Gao et al. [19], Park and Min [36], Duan and Kwok [16] and Xia and Zeng [51] adopted: (1) a set of parallel continuous smooth joint contacts to represent the weak planes, and (2) the parallel bonded contacts to simulate the rock matrix to reveal the mechanical behaviors of transversely isotropic rocks with different micro-structures and micro-parameters. Based on the platform of Universal Distinct Element Code [25], the rock matrix is characterized by a plastic constitutive law and weak planes are described by explicit joints by Debecker [15] and Tan et al.

[46] to study the fracturing features of transversely isotropic rocks.

The use of discontinuum-based methods is limited when dealing with complex and large-scale engineering applications due to greater computational requirements and longer computation times compared to continuum-based methods. Thus, some continuum-based constitutive models, mostly based on the equivalent continuum methods (i.e., the effect of weak planes is diffused into each rock matrix element and each element can describe both the failure of rock matrix and weak planes), have been put forward to address this issue. For example, Zhou et al. [59] proposed an enhanced equivalent continuum model for layered rock mass incorporating bedding structure and stress dependence. Xu et al. [55] introduced the yield approach index into a transversely isotropic elastic–plastic model to estimate the yield degree of layered rock mass. Ismael and Konietzky [23] put forward a constitutive model for inherently anisotropic rocks based on the Hoek and Brown failure criterion. These models have several features such as: (1) the elastic matrix and the strength are transversely isotropic; (2) the yielding behavior can be non-linear and (3) the maximum tensile-stress criterion is introduced in the rock matrix and the weak planes.

For transversely isotropic rocks, significant strain-softening behavior in the post-failure stage has been observed [34, 35, 58]. Thus, an ideal model for layered rock mass should also be able to describe the post-failure behavior. Numerous models have been proposed to describe the strength-weakening effect in the strain-softening stage for isotropic rocks. Examples are: (1) the use of linear strength reduction with the growth of strain in the softening stage

and constant strength in the residual stage [13, 31, 48]; and (2) the use of damage evolution function to describe the deterioration process of the rock due to micro-fracture propagation [28, 38, 52]. However, to the authors' knowledge, research regarding the damage-induced strain-softening behavior of transversely isotropic rocks remains quite limited [10, 11, 55]. In these papers, a scalar anisotropy parameter, which is related to stress invariants and structure orientation tensors, was adopted to reflect the anisotropic behavior of rocks, and scalar internal variable was introduced to account for the material softening. These models have a strong theoretical basis and can retain mathematical rigor. However, the formulations of such models are complex compared to other phenomenological models, which limits their applications in complex engineering problems to some extent. Thus, it is essential to put forward a constitutive model which can describe the strain-softening and damage behavior of transversely isotropic rocks containing weakness planes and deploy such model in practical engineering application.

In this article, a constitutive model is developed to provide a direct representation of the anisotropic and damage behavior of rocks. The aims of the present study are to: (1) Establish an elastic–plastic model to reflect the transverse isotropy in rock deformation and strength based on the Mohr–Coulomb and maximum tensile-stress failure criteria; (2) Introduce a statistical damage evolution rule into the elastic–plastic model to describe the damage and strain-softening behavior of rocks and (3) Demonstrate the use of the model in engineering applications by implementing the model in the computer code FLAC3D [26] to study the non-uniform mechanical response of the surrounding rock and the secondary lining in tunnels situated in a weak layered rock mass.

2 Mechanical properties of transversely isotropic rocks

A summary of test results of transversely isotropic rocks from the literature is given in Table 1, which indicates that the “U” type rocks account for about 71.2% of the total samples, and the proportion of the “wavy” type rocks is the least with magnitude of 5.1%. The following two indices are adopted to evaluate the degree of transverse strength anisotropy:

$$k_1 = \frac{\sigma_{max}}{\sigma_{min}} \quad (1)$$

$$k_2 = \frac{\sigma_0}{\sigma_{90}} \quad (2)$$

where σ_{max} , σ_{min} , σ_0 and σ_{90} (in MPa) are the maximum strength, the minimum strength and the strength at $\theta = 0^\circ$ and $\theta = 90^\circ$, respectively.

Based on the test results of nine kinds of shale specimens, Cheng et al. [7] obtained four types of curves regarding the relation between k_1 and confining pressures. Five types of $k_1 \sim$ confining pressure curves and three types of $k_2 \sim$ confining pressure curves have been classified by Xu [54] based on the test results in the existing literature. Thus, the number of rocks is increased to 39 to validate the former classification (Table 1). The statistical analysis shows that the former classification has general applicability. Specifically, three trends about the changing trends of k_1 with the increase of the confining pressure can be found (Fig. 2): (1) Trend T_{k1-1} : k_1 undergoes a slight decrease of less than one with the increase of the confining pressure; (2) Trend T_{k1-2} : k_1 shows a decrease of larger than one with the increase of the confining pressure; and (3) Trend T_{k1-3} : k_1 remains nearly constant over the entire interval.

In addition, three trends can be categorized regarding the changing trends of k_2 with the increase of the confining pressure (Fig. 3): (1) Trend T_{k2-1} : k_2 undergoes a slight increase of less than one with the increase of the confining pressure; (2) Trend T_{k2-2} : k_2 shows a slight decrease less than one with the increase of the confining pressure, and (3) Trend T_{k2-3} : k_2 remains nearly constant over the entire interval.

3 An equivalent continuum model for the transversely isotropic rocks

This section presents the formulation of the equivalent continuum model for the transversely isotropic rocks that considers experimental observations discussed above.

3.1 Basic assumptions

The equivalent continuum model meets the following assumptions: (1) The transversely isotropic rock comprises rock matrix and weak planes and the influence of weak planes is diffused into the rock matrix. In addition, the rock matrix or the weak plane is described with its own plastic criterion; (2) The elastic deformation of rocks obeys transverse isotropy, that is, the elastic properties of rocks in all directions are the same along the plane parallel to the weak planes but different perpendicular to the weak planes; (3) The rock matrix and weak planes follow the same damage evolution law.

Table 1 Results of triaxial compression test on transversely isotropic rocks

Number	Rock lithology	Type of strength curve	Weak planes-loading angle (°)	Confining pressure (MPa)	Anisotropy indices		References
					k_1	k_2	
1	Xiangxi sandstone	Shoulder	0, 15, 30, 45, 60, 75, 90	0, 5, 10, 15, 20	T_{k1-1}	T_{k2-3}	[14]
2	Quartz sandstone		0, 30, 45, 60, 90	0, 5, 20, 30, 50	T_{k1-1}	T_{k2-1}	[37]
3	Green river shale I		0, 15, 20, 30, 40, 60, 75, 90	7, 34, 69, 103, 172	T_{k1-1}	T_{k2-2}	[47]
4	Green river shale II		0, 15, 20, 30, 40, 60, 75, 90	7, 34, 69, 103, 172	T_{k1-1}	T_{k2-2}	
5	Hunan sandstone		0, 22.5, 45, 67.5, 90	0, 20, 40, 60	T_{k1-1}	T_{k2-1}	[58]
6	Domomitic limestone		0, 10, 20, 30, 40, 50, 60, 70, 80, 90	20, 40, 60, 80	T_{k1-1}	T_{k2-2}	[12]
7	Intra-reservoir marl		0, 15, 30, 45, 60, 75, 90	3, 14, 21	T_{k1-2}	T_{k2-3}	
8	Synthetic rock		0, 15, 30, 45, 60, 75, 90	0, 5, 10, 15	T_{k1-2}	T_{k2-2}	[56]
9	Pengshui shale		0, 30, 60, 90	0, 10, 20, 30	T_{k1-1}	T_{k2-3}	[21]
10	Longmaxi shale II	U	0, 15, 30, 45, 60, 75, 90	0, 10, 30, 45, 60	T_{k1-1}	T_{k2-2}	[22]
11	Carbonaceous phyllite		0, 45, 60, 90	0, 10, 20, 30	T_{k1-3}	T_{k2-3}	[8]
12	Isfahan schist		0, 30, 45, 60, 90	0, 7, 15	T_{k1-1}	T_{k2-3}	[18]
13	Quartzitic schist		0, 15, 30, 45, 60, 75, 90	5, 15, 35, 50, 100	T_{k1-1}	T_{k2-1}	[34]
14	Chlorite schist		0, 15, 30, 45, 60, 75, 90	5, 15, 35, 50, 100	T_{k1-2}	T_{k2-1}	
15	Tournemire shale		0, 20, 30, 45, 60, 75, 90	1, 5, 20, 40, 50	T_{k1-1}	T_{k2-1}	[35]
16	Jiujiang slate		0, 15, 30, 45, 60, 75, 90	0, 5, 10, 15, 20	T_{k1-1}	T_{k2-2}	[10]
17	Martinsburg slate		0, 15, 30, 45, 60, 75, 90	3.5, 10.5, 35, 50, 100	T_{k1-2}	T_{k2-1}	[47]
18	Austin slate		0, 10, 20, 30, 40, 50, 60, 70, 80, 90	35, 67, 138, 207, 276	T_{k1-1}	T_{k2-3}	
19	Penrhyn slate		0, 15, 30, 45, 60, 75, 90	0, 14, 28, 55	T_{k1-2}	T_{k2-3}	
20	Black shale		0, 30, 45, 60, 90	0, 10, 20, 30, 40, 50	T_{k1-1}	T_{k2-2}	[4]
21	Moretown phyllite		0, 15, 30, 45, 60, 75, 90	50, 100, 200	T_{k1-1}	T_{k2-3}	[42]
22	Qingda slate		0, 30, 60, 90	0, 10, 20, 40, 60	T_{k1-3}	T_{k2-2}	[20]
23	Seal shale		0, 15, 30, 45, 60, 75, 90	3, 7, 14, 21, 35	T_{k1-2}	T_{k2-1}	[12]
24	Bituminous coal		0, 15, 30, 45, 60, 75, 90	0, 4, 14, 21	T_{k1-2}	T_{k2-1}	
25	Bossier shale		0, 15, 30, 45, 60, 75, 90	0, 6.89, 20, 41.3, 68.9	T_{k1-2}	T_{k2-1}	[3]
26	Muerta shale		0, 30, 60, 90	0, 6.89, 17.2, 34.5, 138	T_{k1-1}	T_{k2-3}	
27	Sandy mudstone		0, 30, 45, 60, 90	0.5, 1, 1.5	T_{k1-1}	T_{k2-3}	[43]
28	Longmaxi black shale		0, 15, 30, 45, 60, 75, 90	0, 20, 40, 60	T_{k1-2}	T_{k2-1}	[22]
29	Graphite schist		0, 30, 45, 60, 75, 90	0, 4, 10, 20	T_{k1-2}	T_{k2-1}	[1]
30	Dry phyllite		0, 15, 30, 45, 60, 75, 90	0, 5, 15, 30, 60	T_{k1-1}	T_{k2-3}	[30]
31	Saturated phyllite		0, 15, 30, 45, 60, 75, 90	0, 5, 15, 30, 60	T_{k1-1}	T_{k2-3}	
32	Dry slate		0, 15, 30, 45, 60, 75, 90	0, 5, 15, 30, 60	T_{k1-1}	T_{k2-3}	
33	Saturated slate		0, 15, 30, 45, 60, 75, 90	0, 5, 15, 30, 60	T_{k1-2}	T_{k2-1}	
34	Dry orthoquartzite		0, 15, 30, 45, 60, 75, 90	0, 5, 15, 30, 60	T_{k1-1}	T_{k2-3}	
35	Saturated Orthoquartzite		0, 15, 30, 45, 60, 75, 90	0, 5, 15, 30, 60	T_{k1-1}	T_{k2-3}	
36	Phyllite		0, 30, 90	10, 20, 30	T_{k1-3}	T_{k2-3}	[53]
37	Tournemire argillite		0, 30, 45, 60, 90	0, 4, 10	T_{k1-1}	T_{k2-2}	[45]
38	Limestone	Wavy	0, 25, 30, 45, 60, 75, 90	0, 7, 14, 28	T_{k1-1}	T_{k2-3}	[47]
39	Pittsburgh shale		0, 15, 30, 45, 60, 75, 90	0, 10, 20, 30	T_{k1-2}	T_{k2-2}	[6]

Some test results are from Table 1 in Xu et al. [54]

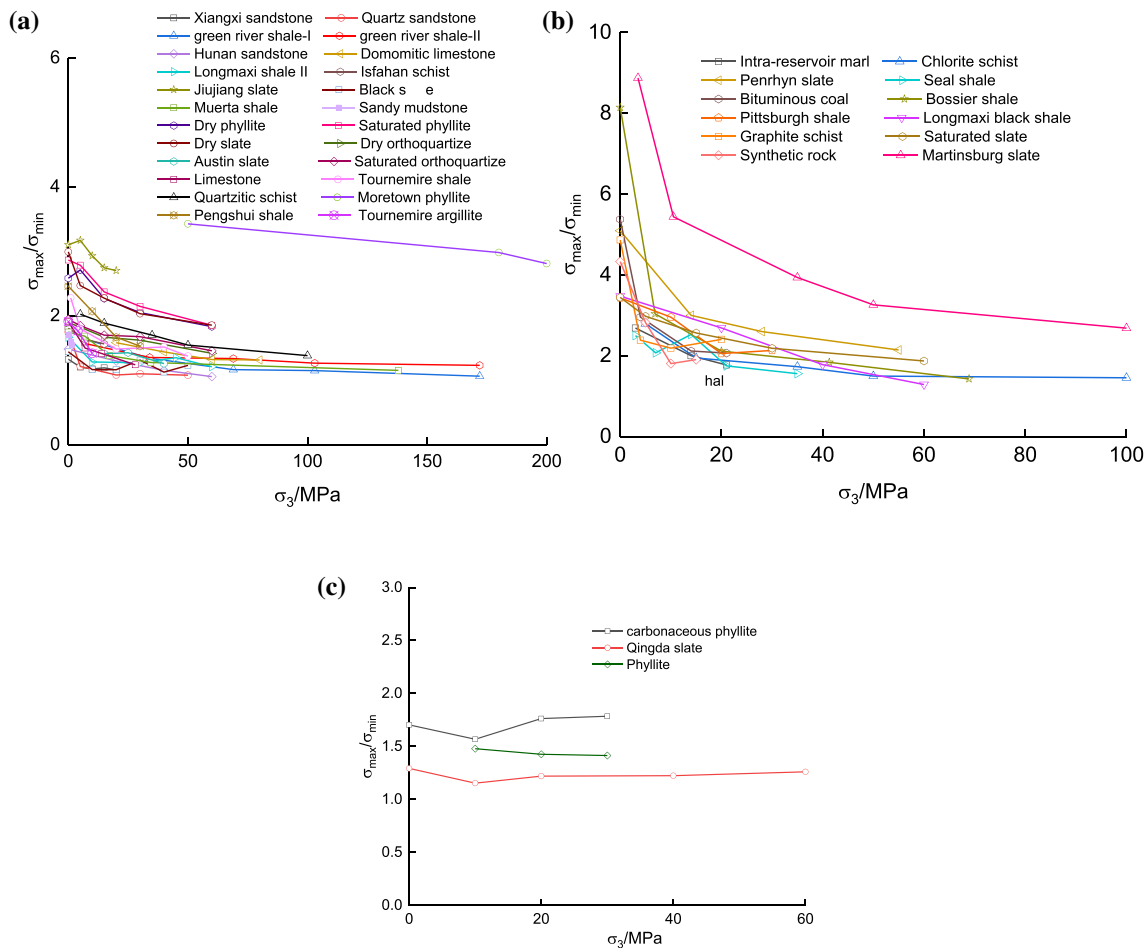


Fig. 2 The changing trends of k_1 with the increase of confining pressure: **a** trend T_{k1-1} ; **b** trend T_{k1-2} ; **c** trend T_{k1-3}

3.2 Elastic behavior

For a transversely isotropic rock, its mechanical response is isotropic at the $x'y'$ plane which is parallel to the weak planes. The coordinate systems are shown in Fig. 4. The elastic behavior of rock in the local coordinate system is:

$$[\sigma'] = [C'][\varepsilon'] \tag{3}$$

where $[\sigma']$, $[\varepsilon']$ and $[C']$ are the stress, strain and stiffness matrix in the local coordinate system, respectively. The stiffness matrix $[C']$ (MPa) is expressed as follows:

$$[C'] = \begin{bmatrix} C'_{11} & C'_{12} & C'_{13} & 0 & 0 & 0 \\ C'_{21} & C'_{22} & C'_{23} & 0 & 0 & 0 \\ C'_{31} & C'_{32} & C'_{33} & 0 & 0 & 0 \\ 0 & 0 & 0 & C'_{44} & 0 & 0 \\ 0 & 0 & 0 & 0 & C'_{55} & 0 \\ 0 & 0 & 0 & 0 & 0 & C'_{66} \end{bmatrix} \tag{4}$$

where $C'_{11} = C'_{22} = \frac{E_1(1-nv_2^2)}{(1+v_1)(1-nv_1-2nv_2^2)}$; $C'_{12} = C'_{21} = \frac{E_1(v_1+nv_2^2)}{(1+v_1)(1-nv_1-2nv_2^2)}$; $n = \frac{E_1}{E_3}$; $C'_{13} = C'_{31} = C'_{23} = C'_{32} = \frac{E_1v_2}{1-v_1-2nv_2^2}$; $C'_{33} = \frac{E_3(1-v_1)}{1-v_1-2nv_2^2}$; $C'_{44} = C'_{55} = \frac{E_1}{1+v_1}$; $C'_{66} =$

$\frac{E_1E_3}{E_1(1+2v_1)+E_3}$; E_1 and v_1 are the elastic modulus (MPa) and Poisson's ratio in the plane of isotropy, respectively; E_3 and v_2 are the elastic modulus (MPa) and Poisson's ratio in the direction normal to the plane of isotropy, respectively.

The elastic behavior of rock in the global coordinate system is

$$[\sigma] = [C][\varepsilon] \tag{5}$$

where $[\sigma]$, $[\varepsilon]$ and $[C]$ are the elastic stress (in MPa), strain and stiffness matrix in the global coordinate system, respectively. The formulation of the stiffness matrix $[C]$ is shown in "Appendix I".

3.3 Plastic behavior

The undamaged Mohr–Coulomb criterion with a tension cut-off was adopted to describe the plastic behavior of the rock matrix (Fig. 5a):

$$f^s = \sigma_1 - \sigma_3N_\phi + 2c\sqrt{N_\phi} \tag{6}$$

$$f^t = \sigma_1 - \sigma_3 \tag{7}$$

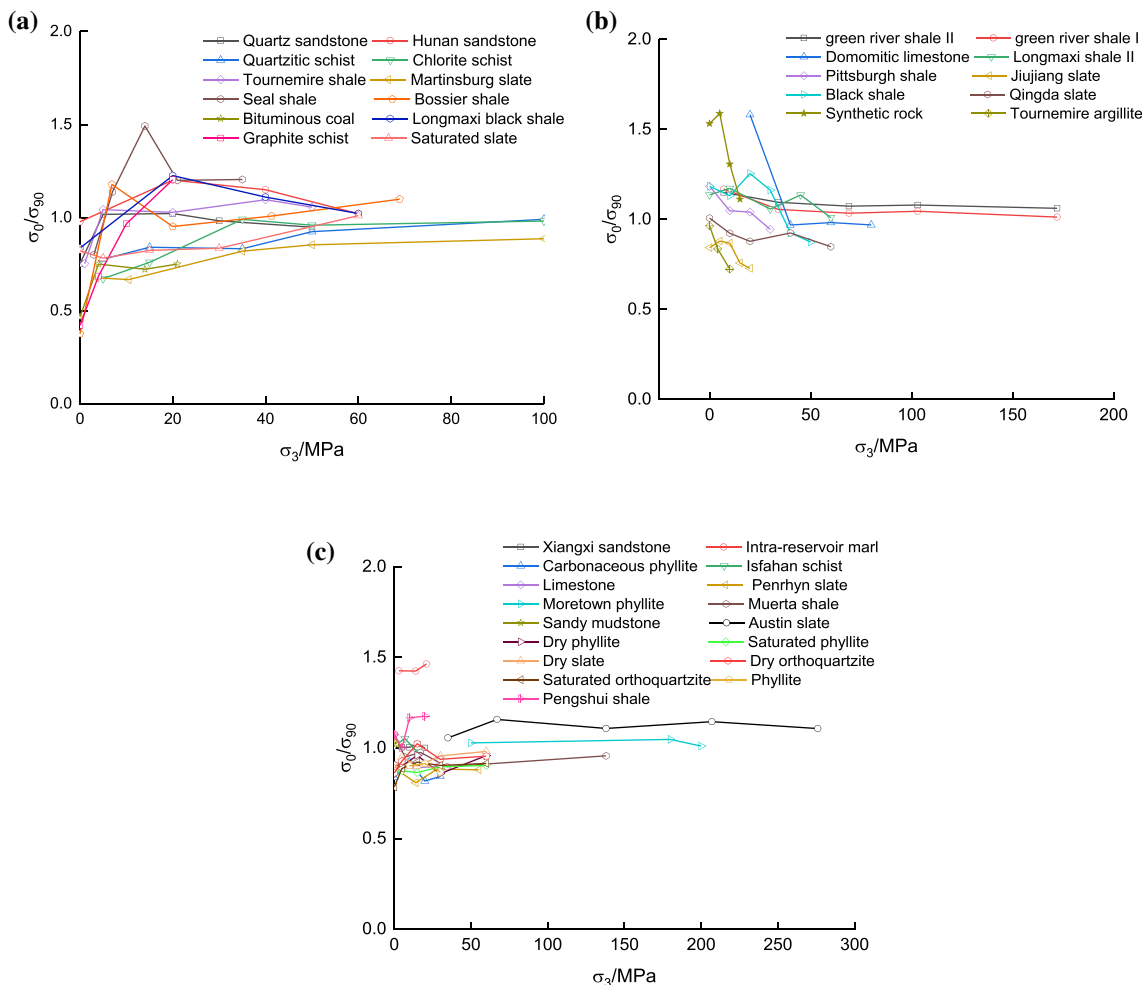


Fig. 3 The changing trends of k_2 with the increase of confining pressure: **a** trend T_{k2-1} ; **b** trend T_{k2-2} ; **c** trend T_{k2-3}

where f^s is the shear yield criterion, f^t is the tensile yield criterion, $N_\varphi = (1 + \sin\varphi)/(1 - \sin\varphi)$, c , φ and σ_t are cohesion (MPa), friction angle ($^\circ$) and tensile strength (MPa) of the rock matrix, respectively.

The corresponding potential functions are:

$$g^s = \sigma_1 - \sigma_3 N_\psi \tag{8}$$

$$g^t = -\sigma_3 \tag{9}$$

where g^s is the shear potential function, g^t is the tensile potential function, $N_\psi = (1 + \sin\psi)/(1 - \sin\psi)$ and ψ is the dilation angle ($^\circ$).

The Mohr–Coulomb criterion with a tension cut-off was also adopted to describe the plastic behavior of the weak planes (Fig. 5b):

$$f_j^s = \tau - \sigma_n \tan \varphi_j - c_j \tag{10}$$

$$f_j^t = \sigma_n - \sigma_j^t; \sigma_{j\max}^t = c_j / \tan \varphi_j \tag{11}$$

where f_j^s is the shear yield criterion, f_j^t is the tensile yield criterion, c_j , φ_j and σ_j^t are cohesion (Pa), friction angle ($^\circ$) and tensile strength (Pa) of weak planes, respectively, $\sigma_{j\max}^t$ is the maximum tensile strength for a weak plane with nonzero friction angle (Pa) and σ_n is the normal stress (Pa) on the weak plane.

The corresponding potential functions are as follows:

$$g_j^s = \tau - \sigma_n \tan \psi_j \tag{12}$$

$$g_j^t = -\sigma_n \tag{13}$$

where g_j^s is the shear potential function, g_j^t is the tensile potential function and ψ_j is the dilation angle of weak planes ($^\circ$).

3.4 Damage behavior

The damaged plastic behavior can be obtained by introducing a damage formulation into the Mohr–Coulomb

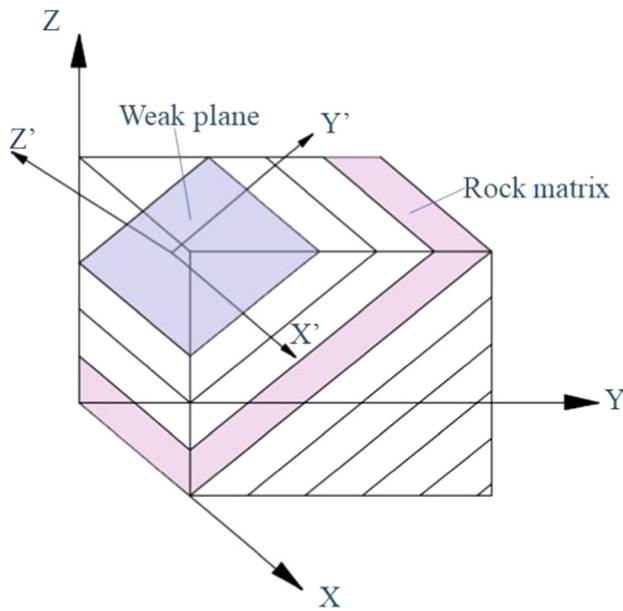


Fig. 4 Coordinate systems of the weak planes and the global reference axes

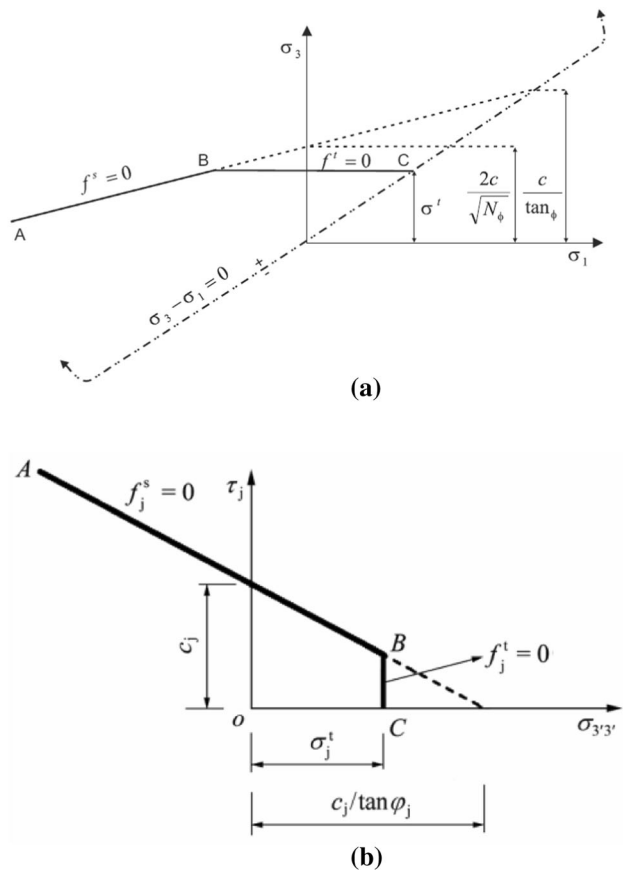


Fig. 5 Yield criterion: **a** rock matrix; **b** weak planes (after Itasca [26])

criterion in Sect. 3.3. The damage evolution law based on Weibull distribution [49] is:

$$D_t = 1 - \exp\left(-\left(\frac{\varepsilon}{\alpha}\right)^m\right) \tag{14}$$

ε is the plastic strain related to the failure pattern of the rocks.

The damage index is defined as:

$$D = 1 - D_t \tag{15}$$

Thus, D corresponds to the probability of survival of rocks, with $D = 1$ corresponding to an undamaged material, and $D = 0$ to a fully damaged material. As rock can undergo either tensile or shear failure, the plastic strain ε , which controls the degree of damage, is defined as follows [26]:

$$\varepsilon = \begin{cases} \frac{2}{3} \sqrt{[(\varepsilon_1^p - \varepsilon_2^p)^2 + (\varepsilon_2^p - \varepsilon_3^p)^2 + (\varepsilon_3^p - \varepsilon_1^p)^2]} & \text{for shear failure} \\ \varepsilon_3^p & \text{for tensile failure} \end{cases} \tag{16}$$

For simplicity, the same damage magnitude D is applied to the evolutions of the cohesion, friction and tensile strength of rocks. Thus, all the plastic parameters vary with the equivalent plastic strains:

$$c_d = Dc, \varphi_d = D\varphi, \sigma_{td} = D\sigma_t \tag{17}$$

$$c_{jd} = Dc_j, \varphi_{jd} = D\varphi_j, \sigma_{td}^j = D\sigma_t^j \tag{18}$$

where c_d , φ_d and σ_{td} are the cohesion (Pa), friction angle ($^\circ$) and tensile strength (MPa) of the rock matrix after damage, respectively, c_{jd} , φ_{jd} and σ_{td}^j are the cohesion (MPa), friction angle ($^\circ$) and tensile strength (Pa) of the weak planes after damage, respectively.

The implementation of the equivalent continuum model for transversely isotropic rocks into the explicit finite different code FLAC3D is presented in the ‘‘Appendix II’’. In the implementation, during a time increment, trial stresses are first calculated; then, a determination is made whether the rock mass will behave only elastically, or in addition to elastic deformation, plastic deformations will occur in the rock matrix, weakness planes or both. The trial stresses are initially obtained assuming elastic loading. If the calculated stress state does not agree with the mode of yielding, then an iteration is performed until there is agreement with the trial and final stresses for a given time increment.

4 Model calibration

As it can be seen, there exists many parameters for the proposed model. Thus, a precise and rapid method determining these parameters is important. The procedures in

the calibration of the parameters (Fig. 6) are outlined as follows [16]:

1. Determine the deformation parameters in the plane of isotropy (E_1 and ν_1) based on the elastic modulus of a specimen with $\theta = 0^\circ$ obtained from the test;
2. Determine the deformation parameters in the direction normal to the plane of isotropy (E_3 and ν_2) based on the elastic modulus of a specimen with $\theta = 90^\circ$ obtained from the test. The other separate equivalent deformation parameter G_{13} (MPa) is obtained from the equation [32]:

$$G_{13} = E_1 E_3 / (E_1 (1 + 2\nu_2) + E_3) \quad (19)$$
3. Determine the rock matrix strength parameters (c , ϕ , σ_t and ψ) and the damage parameters (α and m) of the rock matrix based on the test result regarding the stress–strain of the specimen with $\theta = 90^\circ$.
4. Calibrate the strength of the weak planes (c_j , ϕ_j , σ_t^j and ψ_j) to fit the strength versus θ curve.

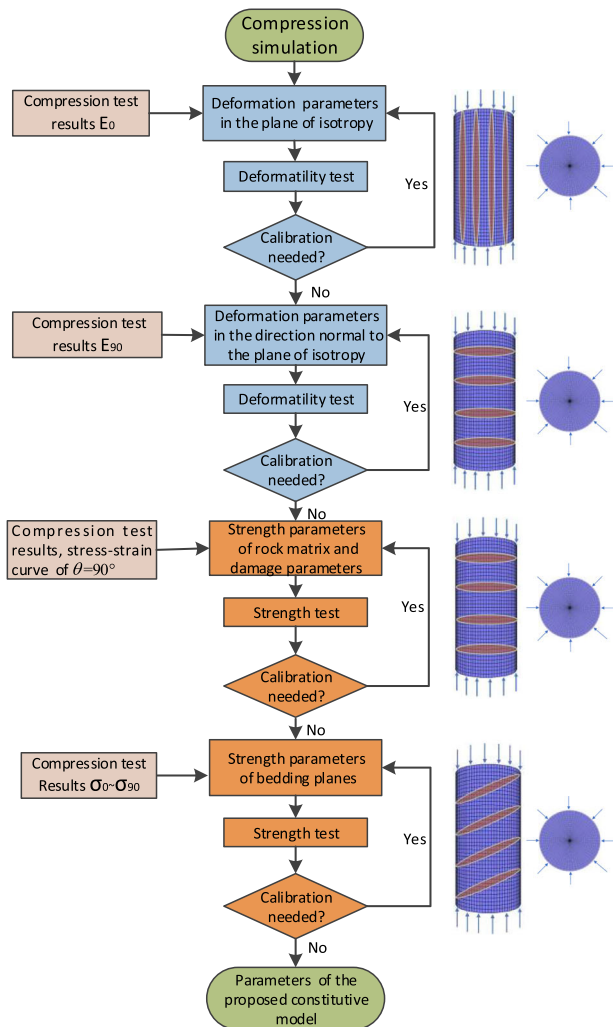


Fig. 6 Model calibration process

Following the above calibration steps, the parameters of three typical rocks with “U” shape (Jiujiang slate, Chen et al. [10]), “shoulder” shape (Longmaxi shale, He et al. [22]) and “wavy” shape (Pittsburgh shale, Cheng et al. [6]) failure trends were calibrated. A cylindrical specimen with diameter of 50 mm and height of 100 mm was built, as shown in Fig. 7. The vertical deformation at the bottom of the specimen was fixed, and the constant vertical displacement at 1×10^{-6} m/step was applied at the top of the specimen for triaxial compression tests. The calibrated parameters are listed in Table 2. Good agreement between numerical simulation and test results in strength and the variation of anisotropic indexes with the increasing confining pressure can be found in Fig. 8.

The numerical simulation and test results regarding the fracture patterns (the localized damaged zones for numerical simulation) and stress–strain curves of Jiujiang slate with different confining pressures are shown in Figs. 9 and 10. Note that the predicted failure patterns were identified by the distribution of damage index, and the damage distribution with a magnitude being less than 0.25 is suitable for identifying rock mass failure. Broadly speaking, several fracturing surfaces along the weak planes occur when rock breaks for $\theta = 0^\circ$, and one fracturing surface along the weak plane occurs when rock breaks for $\theta = 15^\circ - 75^\circ$, and one oblique fracturing surface passing through the specimen occurs when rock breaks for $\theta = 90^\circ$. Figure 10 shows that the simulated stress–strain curves agreed well with the test results, even for the post-failure stages, which indicate that the proposed model can describe the anisotropy in the deformation and strength, and the strain-softening behaviors of transversely isotropic rocks.

In addition, the modelling results also show that the transverse isotropy of rocks is affected by the confining

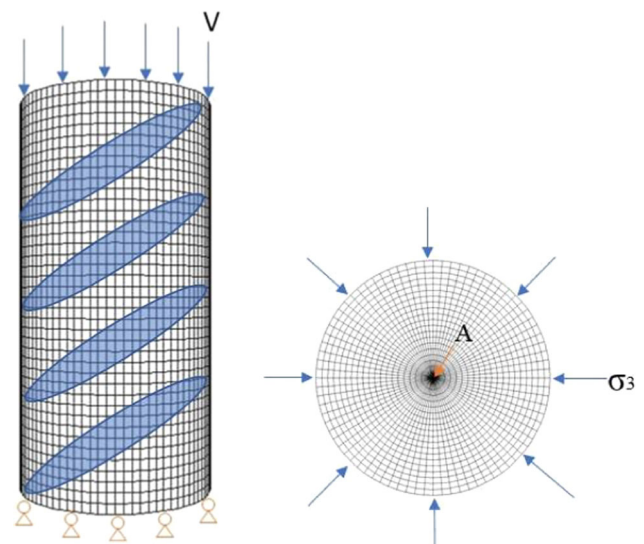


Fig. 7 FLAC3D discretization of a triaxial compression test specimen

stress. The reason is that, although the initial yield and plastic potential functions are linear and the plastic parameters do not depend on the confining stress, the yield and plastic potential functions will become non-linear, and the plastic parameters will become strain-dependent after the occurrence of damage. Thus, the confining stress dependency in transverse isotropy can also be reflected in this model.

5 Application to tunneling

5.1 Background of the project

The Wenchuan–Maerkang Highway [9] is situated in the northwestern part of Sichuan province, China. Metamorphic soft rocks are widely distributed in this region due to the strong uplift and extrusion. The Zhegu mountain tunnel [53] is two-way, four-lane, separated tunnel with width of 13.4 m and height of 10.5 m. The length and maximum buried depth of Zhegu mountain tunnel is 8784 m and 1340 m, respectively. Figure 11a reveals that the tunnel passes through strata consisting of carbonaceous phyllite, carbonaceous slate and metamorphic sandstone. The foliation planes of the carbonaceous phyllite are extremely developed, and the dip angles are about 0° – 60° . The supporting structures are shown in Fig. 11b. Due to the

influence of the weak planes, non-uniform large deformations, such as the invasion of rock mass, cracking of shotcrete, and distortion of the steel arches, appear frequently when the tunnel passes through the phyllite stratum [9].

5.2 Field measurements

Pressure cells, steel strain gauges and concrete strain gauges were installed to measure the rock pressure born by the secondary lining, the strain of the steel arch and the strain of the secondary lining, respectively (Fig. 11c). The inner forces of the steel arch and secondary lining can be calculated as follows:

$$M = \frac{W}{2} E(\varepsilon_i - \varepsilon_e) \quad (20)$$

$$N = \frac{A}{2} E(\varepsilon_i + \varepsilon_e) \quad (21)$$

where M and N are the bending moment (N·m) and axial force (N), respectively, A , E and W are the area (m^2), elastic modulus (MPa) and bending stiffness (m^3), respectively, ε_i and ε_e are the strains of the inner and external surfaces respectively.

For the section of Zhegu mountain tunnel with β (β is the inclination angle of weak planes) of 30° or 60° , the rock pressure and the inner forces were both asymmetrically

Table 2 Model rock parameters used in FLAC3D

Parameter	Jiujiang slate	Longmaxi shale	Pittsburgh shale	Phyllite
<i>Elastic parameters</i>				
E_1 (GPa)	30	34	24	15
E_3 (GPa)	18	16	15	8.25
G_{13} (GPa)	8.9	8.3	7.1	4.1
μ_1	0.22	0.21	0.22	0.21
μ_2	0.21	0.23	0.24	0.23
<i>Plastic parameters</i>				
c (MPa)	20	24	16	12
φ ($^\circ$)	36	33	23	16
σ_t (MPa)	1.6	1.8	1.3	0.9
Ψ ($^\circ$)	10	12	8	5
c_j (MPa)	10	17	7	7.2
φ_j ($^\circ$)	16	26	12	9.6
σ_j^t (MPa)	0.7	0.5	0.4	0.54
Ψ_j ($^\circ$)	6	7	5	3
<i>Damage parameters</i>				
α	0.08	0.03	0.2	0.015
m	0.4	0.6	1.2	0.3

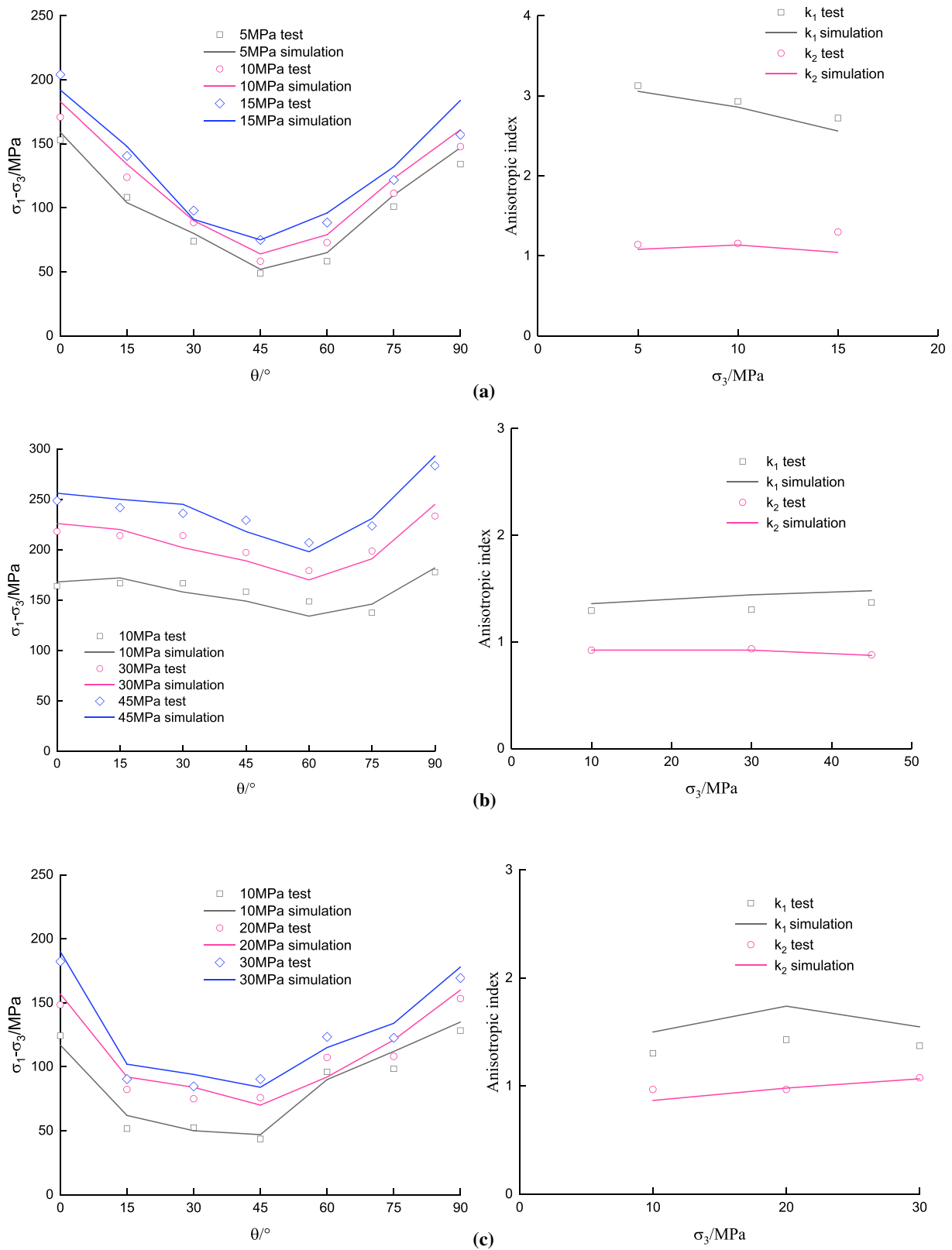


Fig. 8 Comparison of strengths from numerical and test results: **a** Jiujiang slate (Chen et al. [10]); **b** Longmaxi shale (He et al. [22]); **c** Pittsburgh shale (Cheng et al. [6])

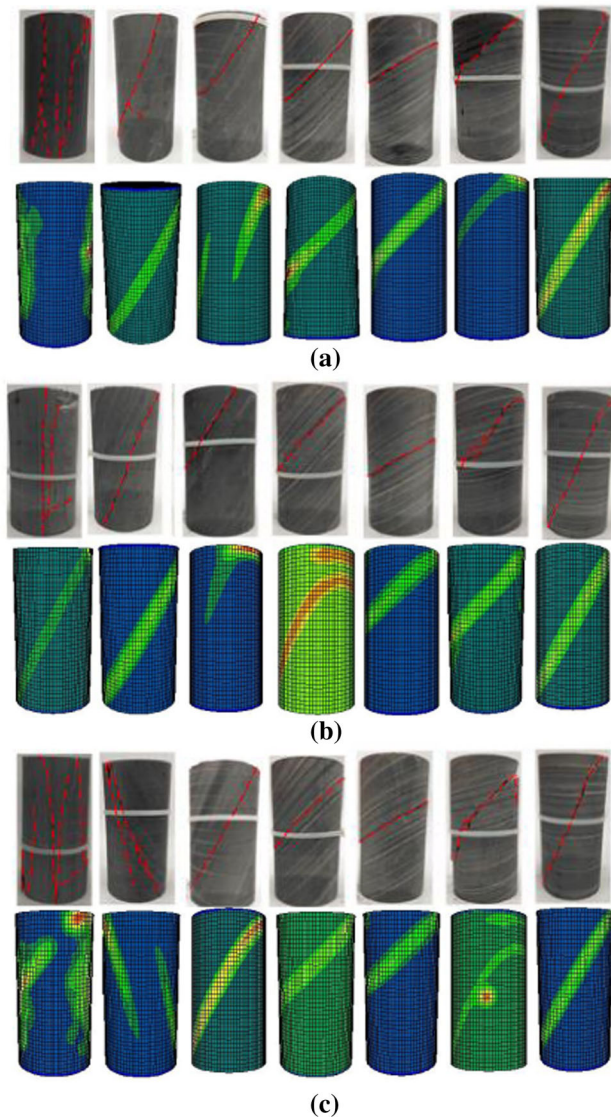


Fig. 9 Comparison of fracture patterns between test results (Chen et al. [10]) and numerical simulation for Jiujiang slate: **a** $\sigma_3 = 5$ MPa; **b** $\sigma_3 = 10$ MPa; **c** $\sigma_3 = 15$ MPa. *Notes:* The highlighted regions of the simulated results indicate the fracturing planes with the damage index being less than 0.25

distributed (Fig. 12). Specifically, the maximum rock pressure occurs near the left spandrel. The bending moment at the left spandrel and right spring line regions are positive with maximum value near the left spandrel, while that at the remaining regions are negative with maximum value near the right spandrel. The distribution of the axial force had an elliptical shape, with the maximum values near the left spring line and right spandrel.

5.3 Numerical model

The Zhegu mountain tunnel is modeled using FLAC3D with a finite difference mesh with dimensions of $80 \text{ m} \times 80 \text{ m} \times 40 \text{ m}$ (in the x , z and y dimensions, respectively), and the results of section at $y = 20 \text{ m}$ is chosen to study the mechanical behavior of the surrounding rock and secondary lining after tunnel excavation, as shown in Fig. 13. The rock bolt, steel arch and shotcrete were represented by a cable element, a beam element, and solid element with the Mohr–Coulomb failure criterion, respectively. The parameters for the different elements are presented in Tables 3, 4 and 5. The secondary lining was represented by the elastic shell elements with E_s of 30 GPa and ν_s of 0.22. The phyllite was simulated using the proposed model, and its parameters are listed in Table 2.

The following values were used in parametric studies of the response of the tunnel:

1. Lateral pressure coefficient: $\lambda = \sigma_y/\sigma_x = 0.5$ ($\sigma_x = 20$ MPa, $\sigma_y = 10$ MPa), $\lambda = 1$ ($\sigma_x = \sigma_y = 20$ MPa), $\lambda = 2$ ($\sigma_x = 10$ MPa, $\sigma_y = 20$ MPa).
2. Inclination angle β : 0° , 30° , 45° , 60° and 90° .
3. Ratio between the stiffness of weak planes and that of rock matrix: 0.3, 0.55 and 0.8.
4. Ratio between the strength of weak planes and that of rock matrix: 0.4, 0.6 and 0.8.

5.4 Simulation results

The main results of the numerical simulations in terms of the different parameters are presented and discussed below.

(1) Effect of the lateral to vertical stress ratio

Taking $\beta = 45^\circ$ as an example, the damage zones of surrounding rock and the inner forces of secondary lining are shown in Fig. 14. The following conclusions can be drawn:

1. For $\lambda = 0.5$, the damage of the surrounding rock is evident in the region from the left spandrel to the right spandrel, and from the invert to the right haunch. For $\lambda = 1$, the damage zones occur at the region from the left haunch to the crown, and from the invert to the right haunch. For $\lambda = 2$, the damage zones happen in the region from the left haunch to the crown, and from the right spring line to the right spandrel. It can be concluded that the damage zones occur in two particular ranges in which the tangent of the tunnel contour was parallel to the direction of the weak planes, and the connecting line of the damage zones (the red line in Fig. 14a) is nearly normal to the weak planes for $\lambda = 1$, while it deflected to the direction of

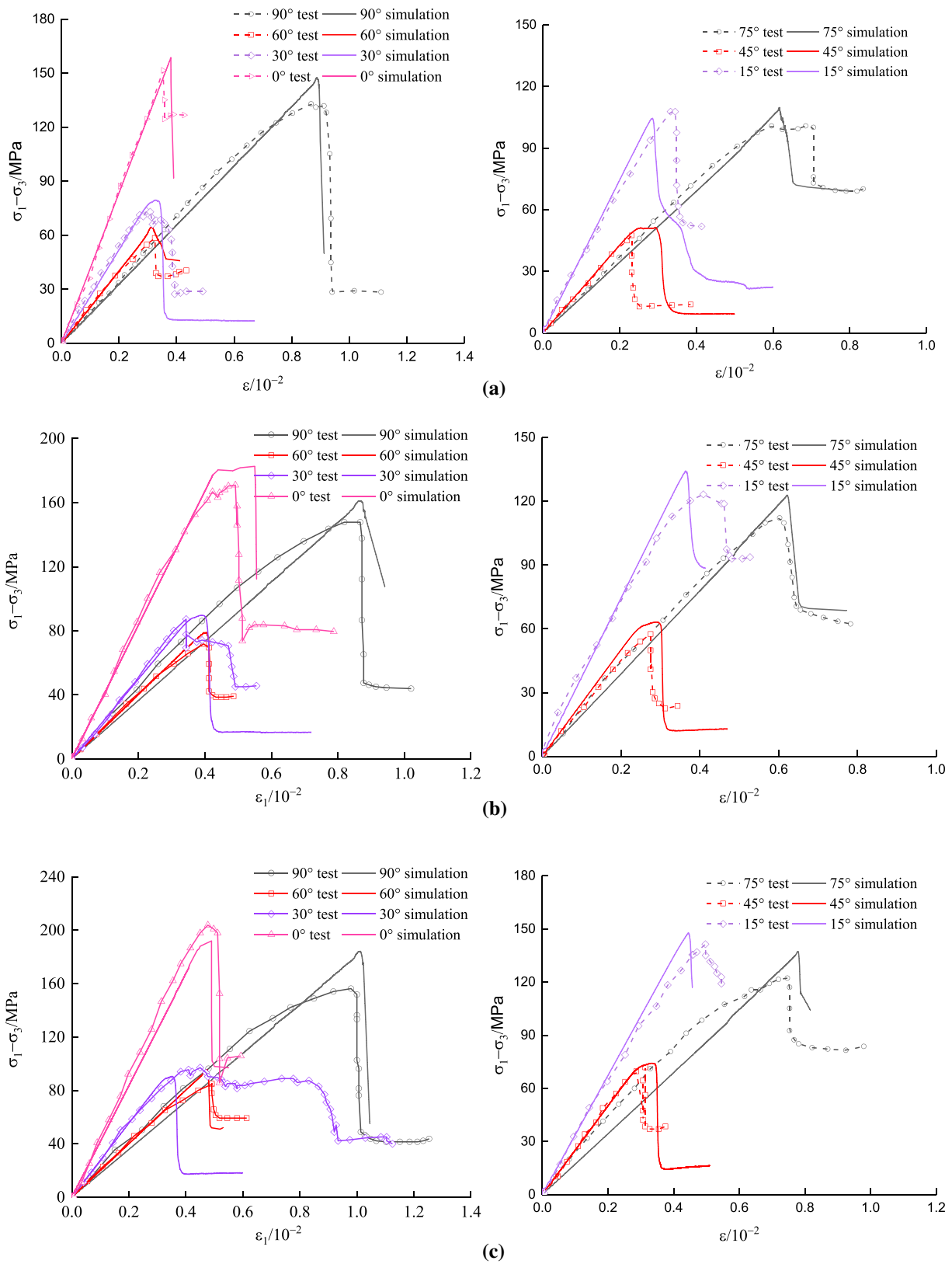


Fig. 10 The stress–strain curves of Jiujiang slate from experiments (Chen et al. [10]) and model simulations: **a** $\sigma_3 = 5$ MPa; **b** $\sigma_3 = 10$ MPa; **c** $\sigma_3 = 15$ MPa

minor principal stress to a certain extent for the non-isotropic geo-stress field. The influence of geo-stress field on the damage zone of surrounding rock may be attributed to the reason that weak planes tend to slide downward along the planes, while the difference of principal stress in vertical and horizontal directions hinders or promotes this movement when $\lambda = 0.5$ and $\lambda = 1$, respectively.

- For $\lambda = 0.5, 1$ and 2 , the bending moment of the secondary lining at the regions of 75° – 150° and 270° – 330° , 85° – 165° and 280° – 350° , and 105° – 180° and 305° – 25° is positive, respectively, while that at the remaining regions are negative. The regions of the positive bending moment are related to the damage zones of the surrounding rock, and the maximum bending moment appears at the section where the connecting line of the damage zones intersects the tunnel contour.
- The axial force is positive (i.e., compression) along the tunnel perimeter with an oval shape, and the maximum value appears at the sections supported by the surrounding rock with few damages, e.g., at 30° and

$180^\circ, 60^\circ$ and 210° , and 85° and 235° for $\lambda = 0.5, 1$ and 2 , respectively.

(2) Effect of weak plane inclination

The damage zones of surrounding rock and the inner forces of secondary lining for different inclination angles ($\lambda = 1$) are shown in Fig. 15. The following conclusions can be drawn:

- The damage region in the surrounding rock is greatly influenced by the inclination angle of the weak planes, and it shows similar distributed features for each angle, that is, the damaged zones are concentrated in certain regions which extend from the tunnel in the direction normal to the weak planes.
- For $\theta = 0^\circ$ or 90° (the weak planes are horizontally or vertically aligned), the inner forces are nearly symmetrically distributed due to the uniform geo-stress and symmetry of the surrounding rock. Specially, for $\theta = 0^\circ$, the maximum axial force appears at the haunch and it is much larger than that at the crown and the invert, while the bending moment is relatively large at the crown and the invert due to the

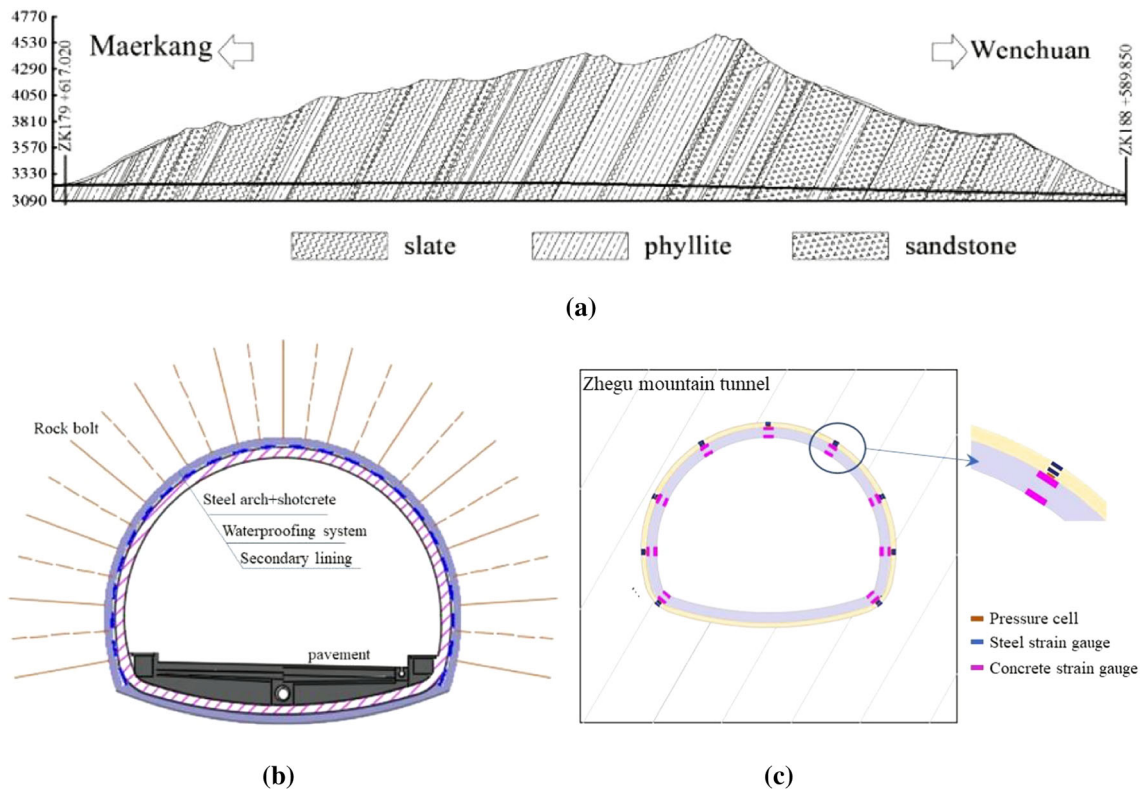


Fig. 11 Zhegu mountain tunnel: **a** longitudinal profile (Chen et al. [9]); **b** supporting structures; **c** layout of sensors

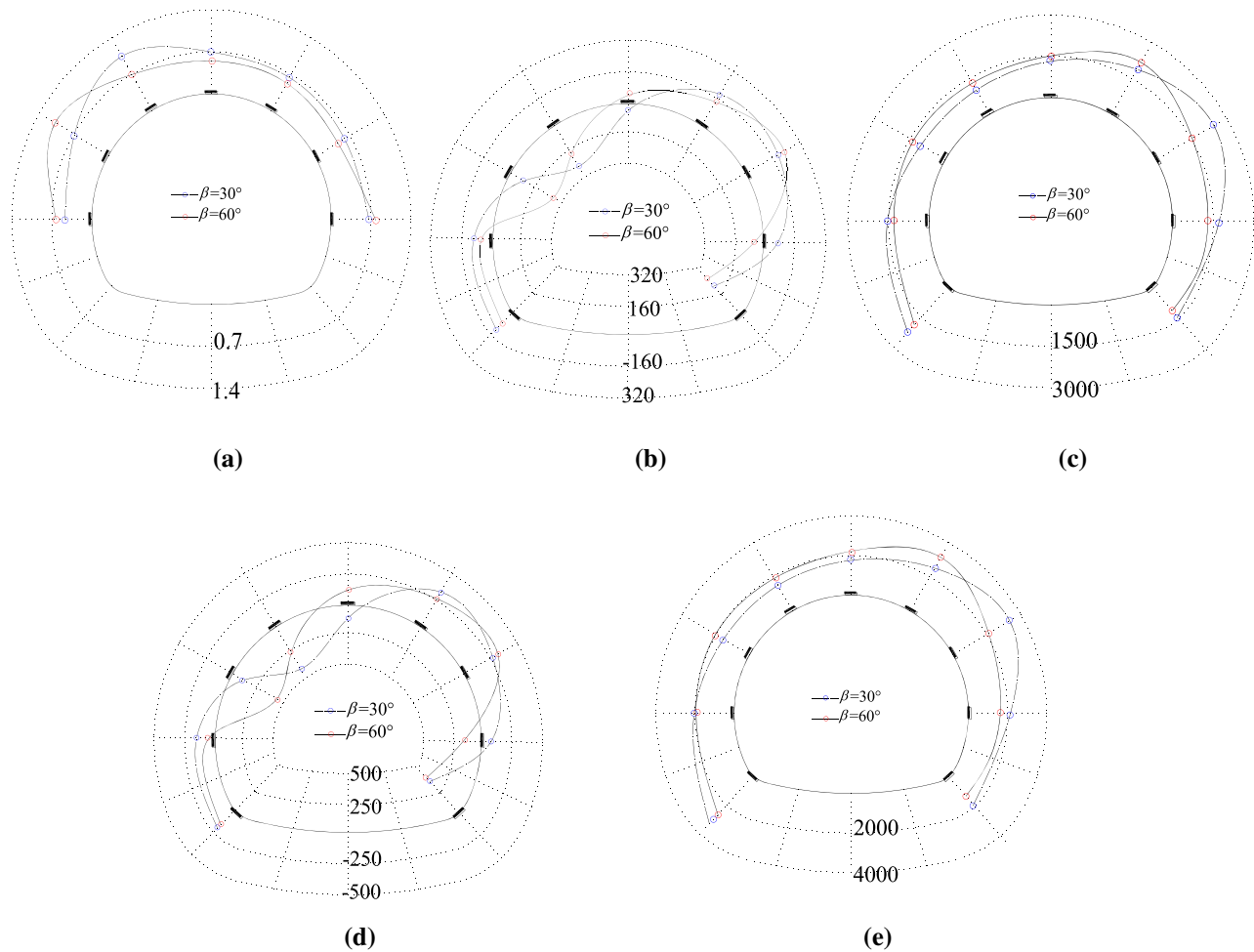


Fig. 12 Measurement results: **a** rock pressure (unit: MPa); **b** bending moment of steel arch (unit: kN-m); **c** axial force of steel arch (unit: kN); **d** bending moment of secondary lining (unit: kN-m); **e** axial force of secondary lining (unit: kN)

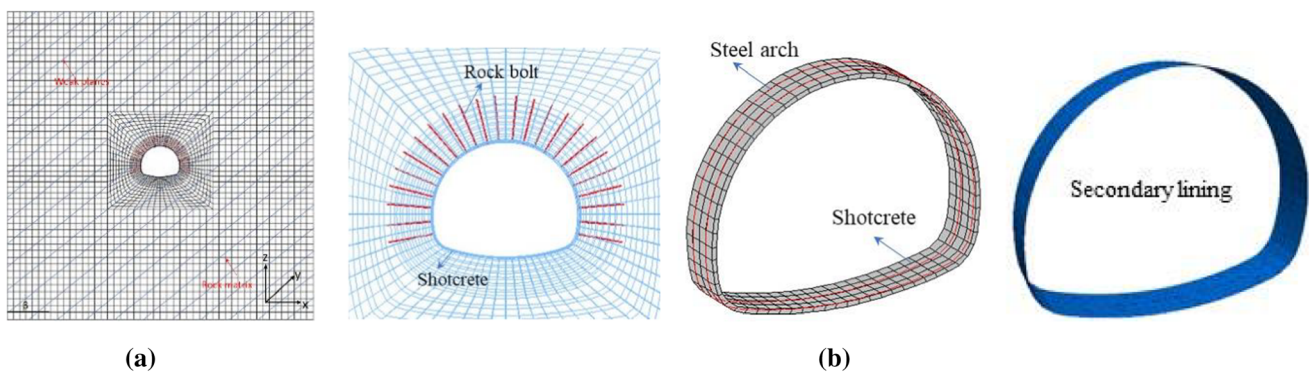


Fig. 13 Numerical model: **a** surrounding rock; **b** supporting structures

damage of the surrounding rock in these regions. For $\theta = 90^\circ$, the maximum axial force occurs at the crown and the invert, and the minimum one appears at the haunch. The bending moment is positive in the region near the left and right haunch, and the invert, and it is negative in the remaining region.

3. For $\theta = 30^\circ$ or 60° , the distributed features of inner forces are similar to those for $\theta = 45^\circ$.
4. As the inclination angle increases, the shapes of the inner forces for the secondary lining change gradually. Increasing the angle from 0 to 90° results in a maximum axial force moving from the haunch to the

Table 3 Rock bolt and grout parameters used in FLAC3D

Rock bolt			Grout		
Diameter (cm)	Yield force F (kN)	Elastic modulus E (GPa)	Bulk modulus k_g (MPa)	Cohesion c (MPa)	Friction angle φ ($^\circ$)
25	127.3	210	20	2	30

Table 4 Steel arch parameters used in FLAC3D

Elastic modulus E (GPa)	Cross sectional area A (cm ²)	Moment of inertia I_x (cm ⁴)	Moment of inertia I_y (cm ⁴)	Ultimate bending moment (kN·m)
210	30.75	1660	123	67.8

Table 5 Shotcrete parameters used in FLAC3D

E (GPa)	ν	σ_t (MPa)	c (MPa)	φ ($^\circ$)
25.5	0.2	1.4	2.3	35

spandrel, and eventually to the crown. On the other hand, the maximum of the positive bending moment eventually moved from the crown to the haunch.

(3) Effect of the stiffness and strength of weak planes

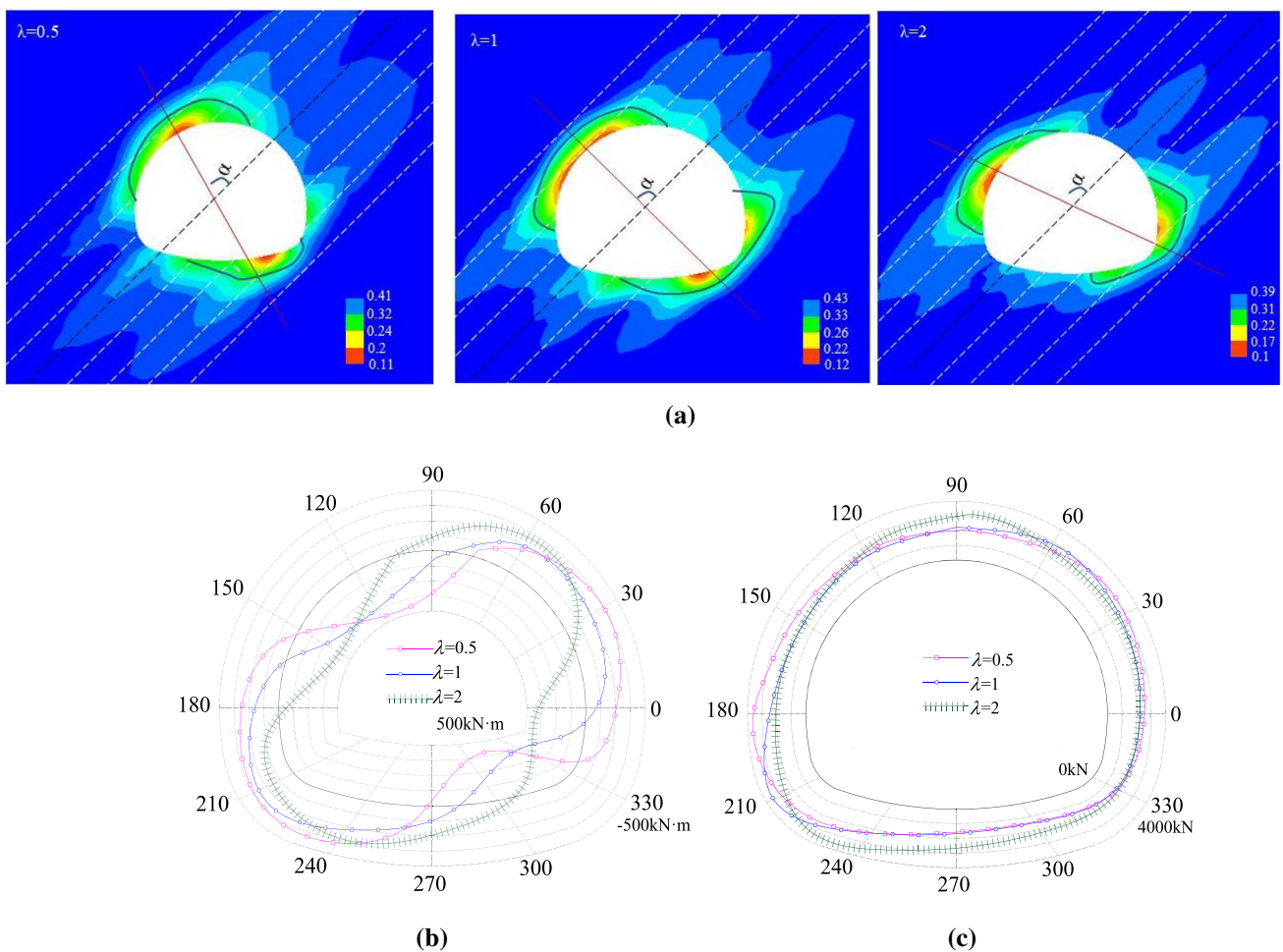


Fig. 14 Effect of the lateral pressure coefficient: **a** damage zones of surrounding rock; **b** bending moment of secondary lining; **c** axial force of secondary lining

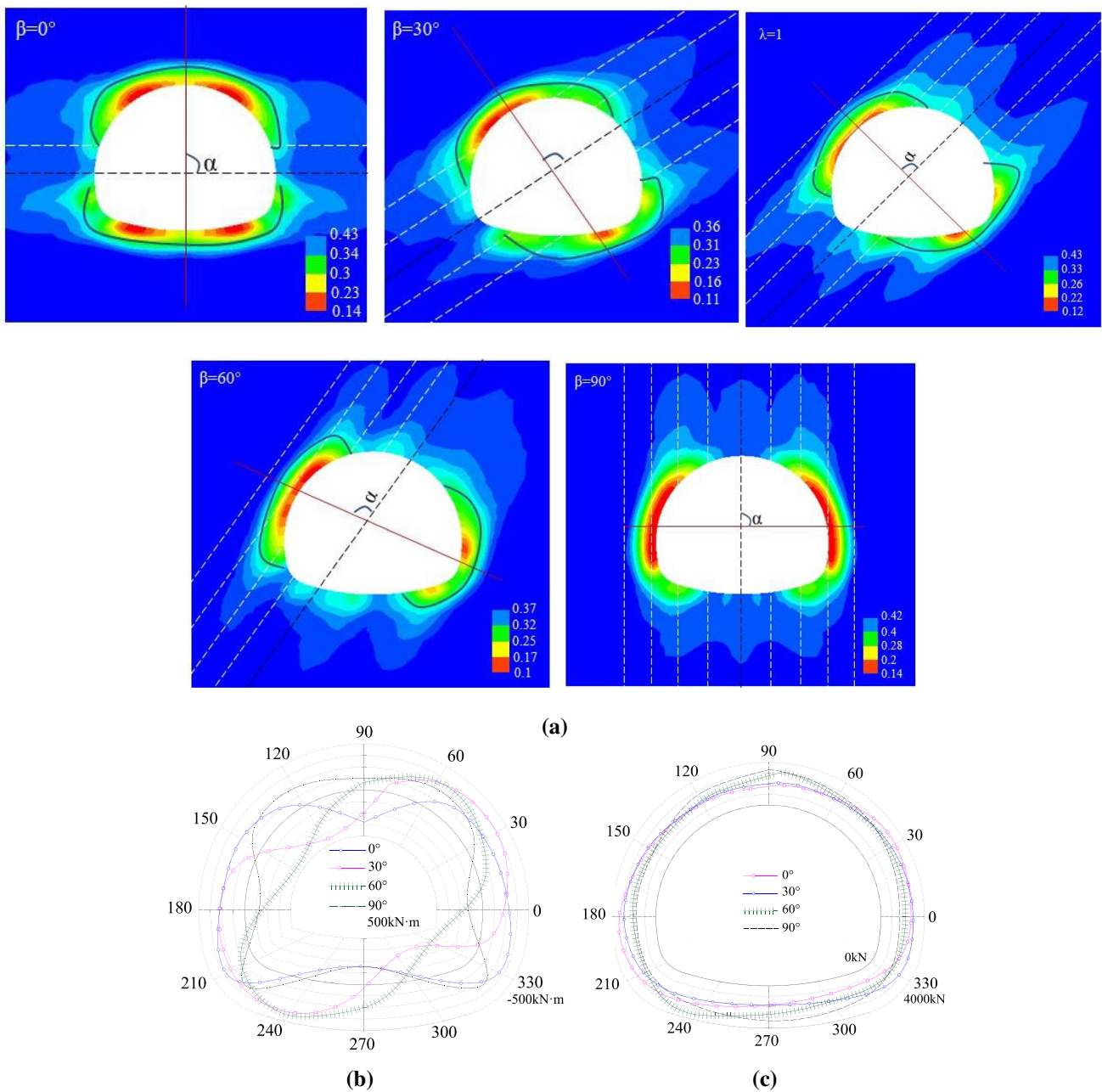


Fig. 15 Effect of inclination angles of weak planes: **a** damage zones of surrounding rock; **b** bending moment of secondary lining; **c** axial force of secondary lining

The mechanical responses of surrounding rock and the inner forces of secondary lining after tunnel excavation for different stiffness or strength of weak planes ($\lambda = 1$, $\beta = 45^\circ$) are shown in Figs. 16, 17. The following conclusions are obtained:

1. With the increase in the stiffness or strength of weak planes, the damage regions of surrounding rock get smaller and their damage degrees decrease. While the distributed features remain the same, e.g., the damaged zones are concentrated in certain regions which extend

from the tunnel in the direction normal to the weak planes for each case.

2. The inner forces get smaller with the increase in the stiffness or strength of weak planes, while their distributed features are similar. The bending moment at the left spandrel and right spring line region are positive with maximum value near the left spandrel, while that at the remaining regions are negative with maximum value near the right spandrel. The distribution of the axial force shows an elliptical shape, with

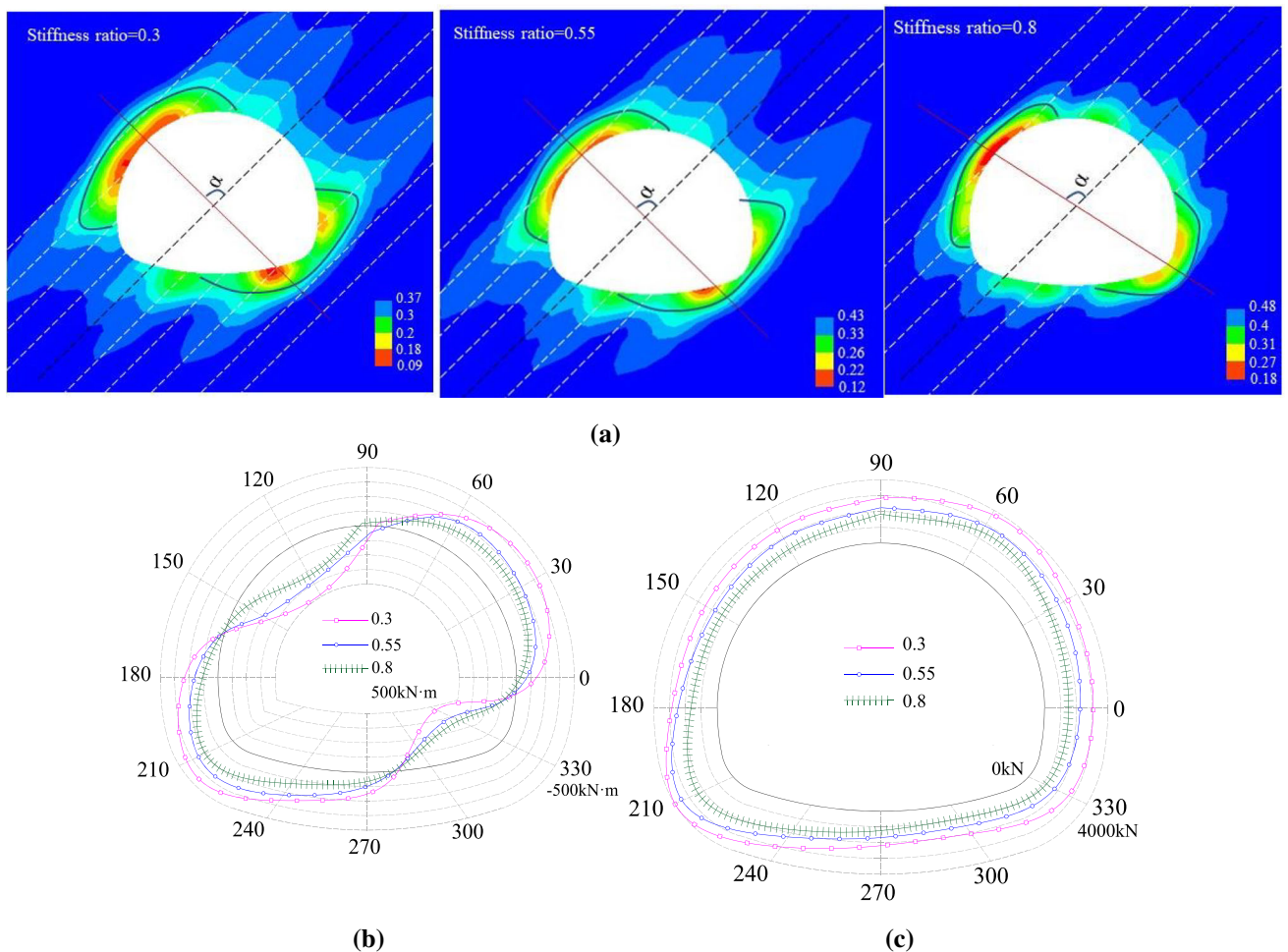


Fig. 16 Effect of the stiffness of weak planes: **a** damage zones of surrounding rock; **b** bending moment of secondary lining; **c** axial force of secondary lining

the maximum values near the left spring line and right spandrel.

The above phenomena indicate that the surrounding rock becomes weaker with the decrease in stiffness and strength of weak planes. Thus, shear sliding and tensile splitting are more likely to emerge on weak planes. The relative movement between fractured weak planes introduces more damaged zones in rock matrix, which result in a larger deformation of surrounding rock and larger inner force of supporting structures as consequence.

6 Conclusion

In this study, an equivalent continuum model for transversely isotropic rocks incorporating nonlinear damage effects was presented. The advantages of this proposed

model are as follows: (1) it can describe the strain-softening behavior of rocks by introducing a statistical damage evolution rule, and (2) it can be adopted to evaluate the safety of practical engineering using a damage index, which is more effective than the plastic zone distribution in identifying the failure of layered rock mass. The validity of the model was verified through the numerical simulation of the conventional triaxial tests. The model was then used to study the non-uniform mechanical responses of the surrounding rock and the secondary lining for a tunnel situated in rock containing weak planes. The main conclusions from the study are summarized as follows:

1. The proposed mode can capture the transverse isotropy in deformation and strength of rocks, and the damage index can represent the failure and fracturing of rocks containing weak planes.

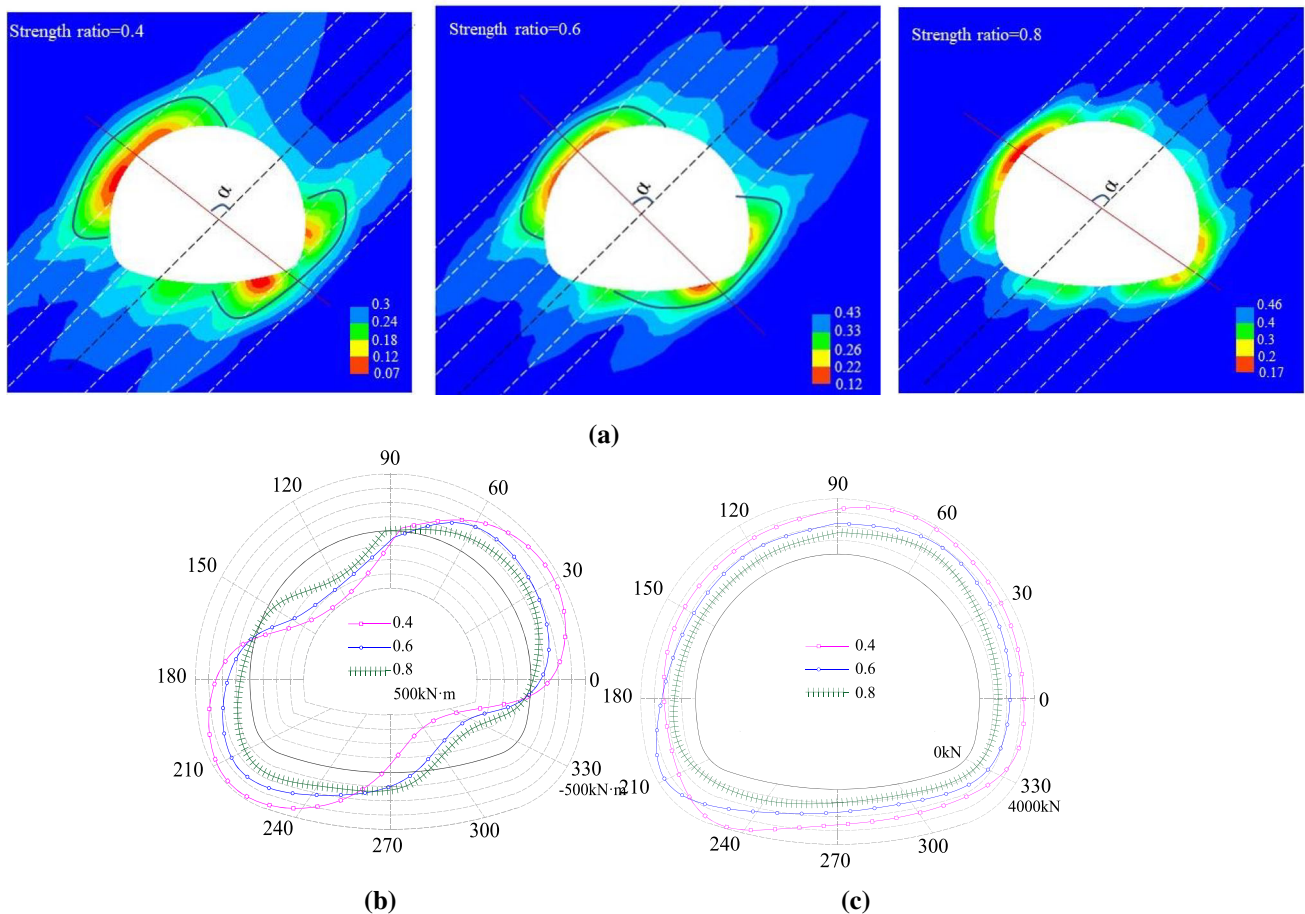


Fig. 17 Effect of the strength of weak planes: **a** damage zones of surrounding rock; **b** bending moment of secondary lining; **c** axial force of secondary lining

- The triaxial compression simulation results from three typical rocks with different directional variations in strength indicate that the fracturing pattern, the failure strength and the stress–strain curves obtained from the proposed model agreed well with the test results. In addition, damage distribution based on the proposed model is effective to identify the failure of layered rock mass.
- The damaged zones of the surrounding rock after tunnel excavation are concentrated in certain regions which extend from the tunnel in the direction normal to the weak planes for each inclination angle, and the connecting line of the damage zones is nearly normal to the weak planes for $\lambda = 1$, while it deflected to the direction of minor principal stress to a certain extent for non-isotropic geo-stress field.
- The distribution of inner forces of the secondary lining shows distinctly asymmetric behaviors, that is, the positive bending moment or larger axial force mainly distributes in the regions where the tangent of tunnel

contour is parallel or vertical to the weak planes, respectively.

- The damage regions of surrounding rock get smaller and their damage degrees decrease, and the inner forces get smaller with the increase in the stiffness or strength of weak planes.

Appendix I: Formulation of stiffness matrix in the global coordinate

The stiffness matrix in the global coordinate $[C]$ is expressed as

$$[C] = [Q][C'][Q]^T \quad (\text{I.1})$$

where $[Q]$ is the transformation matrix defined as follows:

where l_i , m_i and n_i ($i = 1, 2, 3$) are the directional cosines of axis x' , y' and z' , respectively. The matrix of directional cosines $[R]$ is

$$[Q] = \begin{bmatrix} l_1^2 & m_1^2 & n_1^2 & 2m_1n_1 & 2n_1l_1 & 2l_1m_1 \\ l_2^2 & m_2^2 & n_2^2 & 2m_2n_2 & 2n_2l_2 & 2l_2m_2 \\ l_3^2 & m_3^2 & n_3^2 & 2m_3n_3 & 2n_3l_3 & 2l_3m_3 \\ l_2l_3 & m_2m_3 & n_2n_3 & m_2n_3 + m_3n_2 & n_2l_3 + n_3l_2 & l_2m_3 + l_3m_2 \\ l_3l_1 & m_3m_1 & n_3n_1 & m_3n_1 + m_1n_3 & n_3l_1 + n_1l_3 & l_3m_1 + l_1m_3 \\ l_1l_2 & m_1m_2 & n_1n_2 & m_1n_2 + m_2n_1 & n_1l_2 + n_2l_1 & l_1m_2 + l_2m_1 \end{bmatrix} \tag{I.2}$$

$$[R] = \begin{bmatrix} l_1 & m_1 & n_1 \\ l_2 & m_2 & n_2 \\ l_3 & m_3 & n_3 \end{bmatrix} = \begin{bmatrix} \sin \alpha \cos \beta & \cos \alpha \cos \beta & -\sin \beta \\ -\cos \alpha & \sin \alpha & 0 \\ \sin \alpha \sin \beta & \cos \alpha \sin \beta & \cos \beta \end{bmatrix} \tag{I.3}$$

where α and β are the dip direction and dip angle of weak planes, respectively.

Thus, final form of the stiffness matrix $[C]$ is:

$$[C] = \begin{bmatrix} C_{11} & C_{12} & C_{13} & C_{14} & C_{15} & C_{16} \\ C_{21} & C_{22} & C_{23} & C_{24} & C_{25} & C_{26} \\ C_{31} & C_{32} & C_{33} & C_{34} & C_{35} & C_{36} \\ C_{41} & C_{42} & C_{43} & C_{44} & C_{45} & C_{46} \\ C_{51} & C_{52} & C_{53} & C_{54} & C_{55} & C_{56} \\ C_{61} & C_{62} & C_{63} & C_{64} & C_{65} & C_{66} \end{bmatrix} \tag{I.4}$$

where the elements of matrix $[C]$ can be calculated based on Eqs. 4, I.2 and I.3.

Appendix II: implementation of the proposed constitutive model in FLAC 3D

The three-dimensional explicit finite difference implementation of the proposed model are outlined in this Appendix.

1. Deformations of the rock matrix

The function $h(\sigma_1, \sigma_3) = 0$, which is represented by the diagonal between the strength envelopes of $f^s = 0$ and $f^t = 0$ in the principal stress plane (Fig. 18a), is defined to determine the model of yielding of rock matrix:

$$h = \sigma_3 - D\sigma_1 + \alpha^p(\sigma_1 - \sigma^p) \tag{II.1}$$

where

$$\alpha^p = \sqrt{1 + N_{\phi d}^2} + N_{\phi d} \tag{II.2}$$

$$\sigma^p = D\sigma_1 N_{\phi d} - 2Dc\sqrt{N_{\phi d}} \tag{II.3}$$

$$N_{\phi d} = (1 + \sin(D\phi))/(1 - \sin(D\phi)) \tag{II.4}$$

If the stress state falls within domain 1, then shear failure occurs, and the new stress is revised using the flow rule derived from g^s . If the stress falls within domain 2, then tensile failure occurs, and the new stress is re-calculated adopting the flow rule derived from g^t .

For shear failure, partial differentiation of Eq. 8 with damage yields

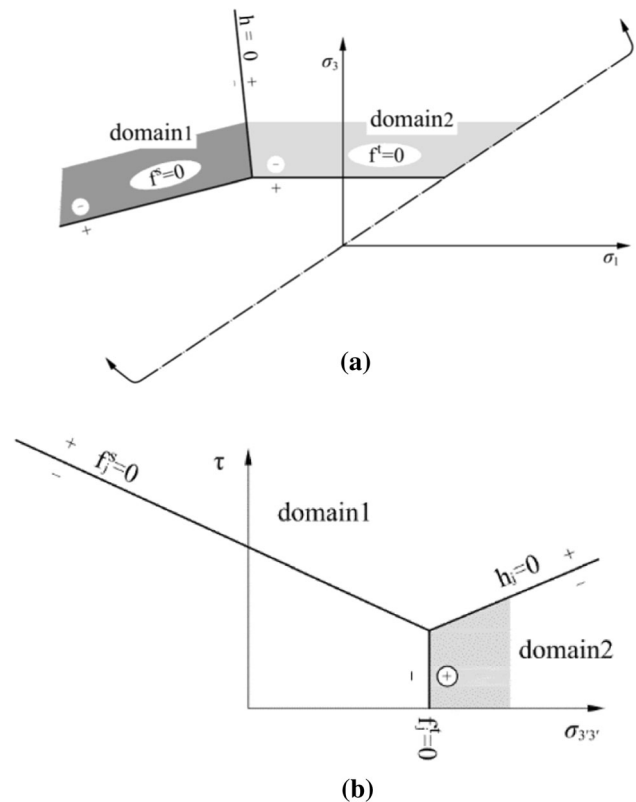


Fig. 18 Determination of yielding type: **a** definition of h and domains used in determining yield type of the rock matrix; **b** definition of h_j and the domains used in determining yield type of the weak planes (after Itasca [26])

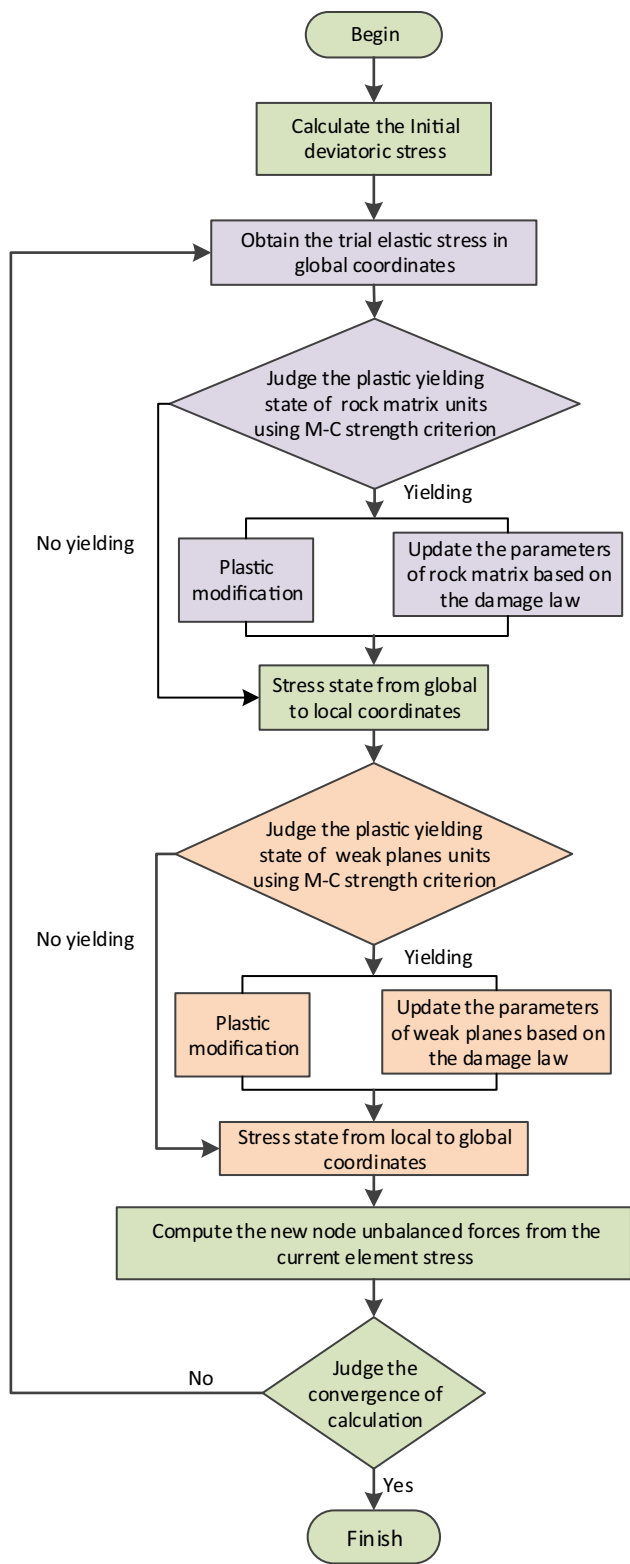


Fig. 19 Flowchart of the implementation of the proposed model

$$\frac{\partial g^s}{\partial \sigma_x} = 1, \frac{\partial g^s}{\partial \sigma_y} = 0, \frac{\partial g^s}{\partial \sigma_z} = -N_\psi, \frac{\partial g^s}{\partial \tau_{xy}} = 0, \frac{\partial g^s}{\partial \tau_{yz}} = 0, \frac{\partial g^s}{\partial \tau_{xz}} = 0 \tag{II.5}$$

Thus, the expressions of the new stress are

$$\begin{aligned} \sigma_x^N &= \hat{\sigma}_x^I - \lambda^*(C_{11} - C_{13}N_\psi) \\ \sigma_y^N &= \hat{\sigma}_y^I - \lambda^*(C_{21} - C_{23}N_\psi) \\ \sigma_z^N &= \hat{\sigma}_z^I - \lambda^*(C_{31} - C_{33}N_\psi) \\ \sigma_{yz}^N &= \hat{\sigma}_{yz}^I - \lambda^*(C_{41} - C_{43}N_\psi) \\ \sigma_{xz}^N &= \hat{\sigma}_{xz}^I - \lambda^*(C_{51} - C_{53}N_\psi) \\ \sigma_{xy}^N &= \hat{\sigma}_{xy}^I - \lambda^*(C_{61} - C_{63}N_\psi) \end{aligned} \tag{II.6}$$

where

$$\lambda^* = \frac{f^s = \sigma_1 - \sigma_3 N_{\phi d} + 2Dc\sqrt{N_{\phi d}}}{(C_{11} - C_{13})N_\psi - (C_{31} - C_{33}N_\psi)N_{\phi d}} \tag{II.7}$$

For tensile failure, partial differentiation of Eq. 9 with damage gives

$$\frac{\partial g^s}{\partial \sigma_x} = 0, \frac{\partial g^s}{\partial \sigma_y} = 0, \frac{\partial g^s}{\partial \sigma_z} = -1, \frac{\partial g^s}{\partial \tau_{xy}} = 0, \frac{\partial g^s}{\partial \tau_{yz}} = 0, \frac{\partial g^s}{\partial \tau_{xz}} = 0 \tag{II.8}$$

Thus, the expressions of the new stress are

$$\begin{aligned} \sigma_x^N &= \hat{\sigma}_x^I - \lambda^* C_{13} & \sigma_y^N &= \hat{\sigma}_y^I - \lambda^* C_{23} \\ \sigma_z^N &= \hat{\sigma}_z^I - \lambda^* C_{33} & \sigma_{yz}^N &= \hat{\sigma}_{yz}^I - \lambda^* C_{43} \\ \sigma_{xz}^N &= \hat{\sigma}_{xz}^I - \lambda^* C_{53} & \sigma_{xy}^N &= \hat{\sigma}_{xy}^I - \lambda^* C_{63} \end{aligned} \tag{II.9}$$

where

$$\lambda^* = \frac{\sigma_{td} - \sigma_{t3}}{(C_{11} - C_{13})N_\psi - (C_{31} - C_{33}N_\psi)N_{\phi d}} \tag{II.10}$$

2. Deformations of the weak planes

The function $h_j(\sigma_1, \sigma_3) = 0$, which is represented by the diagonal between the strength envelope of $f_j^s = 0$ and $f_j^t = 0$ in the principal stress plane (Fig. 18b), is defined:

$$h_j = \tau - \tau_j^p - \alpha_j^p(\sigma_n - \sigma_j^t) \tag{II.11}$$

where

$$\tau_j^p = Dc_j - \tan(D\phi_j)D\sigma_j^t \tag{II.12}$$

$$\alpha_j^p = \sqrt{1 + \tan(D\phi_j)^2} - \tan(D\phi_j) \tag{II.13}$$

If the stress falls within domain 1, then shear failure occurs, and the new stress is revised using the flow rule derived from g_j^s . If the stress falls within domain 2, then tensile failure occurs, and the new stress is re-calculated adopting the flow rule derived from g_j^t .

For shear failure, partial differentiation of Eq. 12 yields

$$\frac{\partial g_j^s}{\partial \sigma_{x'}} = 0, \frac{\partial g_j^s}{\partial \sigma_{y'}} = 0, \frac{\partial g_j^s}{\partial \sigma_{z'}} = \tan \psi_j, \frac{\partial g_j^s}{\partial \tau} = 1 \quad (\text{II.14})$$

Thus, the expressions of the new stress are

$$\begin{cases} \sigma_{x'}^N = \sigma_{x'}^I - \lambda^s C_{13} \tan \psi_j \\ \sigma_{y'}^N = \sigma_{y'}^I - \lambda^s C_{13} \tan \psi_j \\ \sigma_{z'}^N = \sigma_{z'}^I - \lambda^s C_{33} \tan \psi_j \\ \tau^N = \tau^I - 2\lambda^s C_{44} \end{cases} \quad (\text{II.15})$$

where

$$\lambda^s = \frac{\tau - \sigma_n \tan(D\phi_j) - Dc_j}{2C_{44} + C_{33} \tan \psi_j \tan(D\phi_j)} \quad (\text{II.16})$$

For tensile failure, partial differentiation of Eq. 13 gives

$$\frac{\partial g_j^t}{\partial \sigma_{x'}} = 0, \frac{\partial g_j^t}{\partial \sigma_{y'}} = 0, \frac{\partial g_j^t}{\partial \sigma_{z'}} = 1, \frac{\partial g_j^t}{\partial \tau} = 0 \quad (\text{II.17})$$

Thus, the expressions of the new and updated stresses are

$$\begin{cases} \sigma_{x'}^N = \sigma_{x'}^I - \lambda^t C_{13} \\ \sigma_{y'}^N = \sigma_{y'}^I - \lambda^t C_{13} \\ \sigma_{z'}^N = \sigma_{z'}^I - \lambda^t C_{33} \end{cases} \quad (\text{II.18})$$

where

$$\lambda^t = \frac{\sigma_n - D\sigma_j^t}{C_{33}} \quad (\text{II.19})$$

The flowchart of the implementation of the proposed model is shown in Fig. 19. The main steps are as follows:

1. Assume that the rock behaves elastically, and the trial stresses in global coordinate are initially obtained.
2. Judge the yielding state of the rock matrix element based on the M-C criterion and modify its stress and strain if it yields. In addition, the plastic parameters of the element will be updated based on the damage evolutionary law.
3. Convert the stress tensor from the global coordinate to the local coordinate and judge the yielding state of the weak plane element based on the M-C criterion and modify its stress and strain if it yields. In addition, the plastic parameters of the element will be updated based on the damage evolutionary law.
4. Steps 1–3 are repeated until convergence of calculation is reached.

Acknowledgements The research presented in this paper was supported by the U.S. Department of Transportation (DOT) under Grant No. 69A3551747118. The opinions expressed in this paper are those of the authors and not of the funding agencies.

References

1. Akai K (1971) The failure surface of isotropic and anisotropic rocks under multiaxial stresses. *J Society Mater Sci Jpn* 20(209):122–128
2. Abousleiman YN, Hoang SK, Liu C (2014) Anisotropic porothermoelastic solution and hydro-thermal effects on fracture width in hydraulic fracturing. *Int J Numer Anal Meth Geomech* 38:493–517
3. Ambrose J. Failure of anisotropic shales under triaxial stress conditions. Dissertation, Imperial College London, 2014.
4. Chen TY, Feng XT, Zhang XW, Cao WD, Fu CJ (2014) Experimental study on mechanical and anisotropic properties of black shale. *Chinese J Rock Mech Eng* 33(9):1772–1779 (in Chinese)
5. Cho JW, Kim H, Jeon SK, Min KB (2012) Deformation and strength anisotropy of Asan gneiss, Boryeong shale, and Yeoncheon schist. *Int J Rock Mech Min Sci* 50:158–169
6. Cheng JY, Wan ZJ, Zhang YD, Li WF, Peng SS, Zhang P (2015) Experimental study on anisotropic strength and deformation behavior of a coal measure shale under room dried and water saturated conditions. *Shock Vib* 5:1–13
7. Cheng C, Li X, Qian HT (2017) Anisotropic Failure Strength of Shale with Increasing Confinement: Behaviors, Factors and Mechanism. *Materials* 10(11):1310
8. Chen ZQ, He C, Wu D, Gan LW, Xu GW, Yang WB (2018) Mechanical properties and energy damage evolution mechanism of deep-buried carbonaceous phyllite. *Rock Soil Mech* 39(2):445–456 (in Chinese)
9. Chen ZQ, He C, Xu GW, Ma GY, Wu Di. A case study on the asymmetric deformation characteristics and mechanical behavior of deep-buried tunnel in phyllite. *Rock Mech Rock Eng.*2019;52:4527–4545.
10. Chen YF, Wei K, Liu W, Hu SH, Hu R, Zhou CB (2016) Experimental characterization and micromechanical modelling of anisotropic slates. *Rock Mech Rock Eng* 49(9):3541–3557
11. Chen L, Shao JF, Huang HW (2010) Coupled elastoplastic damage modeling of anisotropic rocks. *Comp Geotech* 37:187–194
12. Crawford BR, DeDontney NL, Alramahi B, Ottesen S. Shear strength anisotropy in fine-grained rocks. In: 46th US rock mechanics/geomechanics symposium, Chicago, IL, USA, 2012.
13. Cui L, Zheng JJ, Dong YK, Zhang B, Wang A (2017) Prediction of critical strains and critical support pressures for circular tunnel excavated in strain-softening rock mass. *Eng Geol* 224:43–61
14. Deng HF, Wang W, Li JL, Zhang YC, Zhang XJ (2018) Experimental study on anisotropic characteristics of bedded sandstone. *Chinese J Rock Mech Eng* 37(1):112–120 (in Chinese)
15. Debecker B (2008) Influence of planar heterogeneities on the fracture behavior of rock. Katholieke Universiteit Leuven, Leuven
16. Duan K, Kwok CY (2015) Discrete element modeling of anisotropic rock under Brazilian test conditions. *Int J Rock Mech Min Sci* 78:46–56
17. Everitt RA, Lajtai EZ (2014) The influence of rock fabric on excavation damage in the Lac du Bonnet granite. *Int J Rock Mech Min Sci* 41:1277–1303
18. Fahimifar A (2004) Strength and deformation properties of a schist rock in Isfahan. *IJST-T Civ Eng* 28:619–622
19. Gao K, Meguid MA, Chouinard LE (2020) On the role of pre-existing discontinuities on the micromechanical behavior of confined rock samples: a numerical study. *Acta Geotech.* [https://doi.org/10.1007/s11440-020-01037-0\(0123456789\)-volIV\(0123456789,-\).volV](https://doi.org/10.1007/s11440-020-01037-0(0123456789)-volIV(0123456789,-).volV)

20. Hao XJ, Feng XT, Li SJ. Study on the anisotropy of mechanical properties of slate. 13th International Congress of Rock Mechanics, Montreal, Canada, 2015.
21. Hong GB, Chen M, Lu YH, Jin Y (2018) Study on the anisotropic characteristic of deep shale in southern Sichuan basin and their impacts on fracturing pressure. *Petroleum Drill Tech* 46:78–85
22. He B, Xie LZ, Li FX, Zhao P, Zhang Y (2017) Anisotropic mechanism and characteristics of deformation and failure of Longmaxi shale. *SCIENTIA SINICA Phys, Mechanica & Astronomica* 47(11):1–12 (in Chinese)
23. Ismael M, Konietzky H (2019) Constitutive model for inherent anisotropic rocks: Ubiquitous joint model based on the Hoek-Brown failure criterion. *Comput Geotech* 105:99–109
24. Itasca consulting group Inc. Particle flow code in 2 dimensions user's guide. 2008; Minneapolis, Minnesota.
25. Itasca consulting group Inc. Universal discrete element code in 2 dimensions user's guide. 2005; Minneapolis, Minnesota.
26. Itasca Consulting Group Inc. FLAC3D User's Manual (version 3.0). 2005; Minneapolis, USA.
27. Jin ZF, Li WX, Jin CR, Hambleton J, Cusatis G (2018) Anisotropic elastic, strength, and fracture properties of Marcellus shale. *Int J Rock Mech Min* 109:124–137
28. Katsuki D, Gutierrez M (2011) Viscoelastic damage model for asphalt concrete. *Acta Geotech* 6:231–241
29. Kim H, Cho JW, Song I, Min KB (2012) Anisotropy of elastic moduli, P-wave velocities, and thermal conductivities of Asan Gneiss, Boryeong Shale, and Yeoncheon Schist in Korea. *Eng Geol* 148:68–77
30. Kumar J. Engineering behavior of anisotropic rocks. Dissertation, IIT Roorkee, Indian, 2006.
31. Lee YK, Pietruszczak S (2008) A new numerical procedure for elasto-plastic analysis of a circular opening excavated in a strain-softening rock mass. *Tunn Undergr Space Technol* 15:187–213
32. Lekhnitskii SG (1981) Theory of Elasticity of an Anisotropic Body. Mir Publishers, Moscow
33. Lisjak A, Grasselli G, Vietor T (2014) Continuum-discontinuum analysis of failure mechanisms around unsupported circular excavations in anisotropic clay shales. *Int J Rock Mech Min Sci* 65:96–115
34. Nasser MHB, Rao KS, Ramamurthy T (2003) Anisotropic strength and deformational behavior of Himalayan schist. *Int J Rock Mech Min* 40(1):3–23
35. Niandou H, Shao JF, Henry JP, Fourmaintraux D (1997) Laboratory investigation of the mechanical behavior of Tournemire shale. *Int J Rock Mech Min* 34(1):3–16
36. Park B, Min KB (2015) Bonded-particle discrete element modeling of mechanical behavior of transversely isotropic rock. *Int J Rock Mech Min Sci* 76:243–255
37. Peng JW, Zeng FT, Li CH, Miao SJ. Experimental study of anisotropy and mechanical property of quartz sandstone. *Rock Soil Mech.* 2017; 38(supp):103–112. (in Chinese)
38. Peng J, Cai M, Rong G, Yao MD, Jiang QH, Zhou CB (2017) Determination of confinement and plastic strain dependent post-peak strength of intact rocks. *Eng Geol* 218:187–196
39. Przecherski P, Pietruszczak S (2020) On specification of conditions at failure in interbedded sedimentary rock mass. *Acta Geotech* 15:365–374
40. Pouragha M, Wan R, Eghbalian M (2019) Critical plane analysis for interpreting experimental results on anisotropic rocks. *Acta Geotech* 14:1215–1225
41. Ramamurthy T. Strength and modulus responses of anisotropic rocks. In: Hudson JA, editor. *Comprehensive rock engineering*, vol. 1. Fundamentals. Oxford: Pergamon Press, 1993:313–329.
42. Saeidi O, Vaneghi RG, Rasouli V, Gholami R (2013) A modified empirical criterion for strength of transversely anisotropic rocks with metamorphic origin. *B Eng Geol Environ* 72(2):257–269
43. Shi H. Laboratory tests and constitutive modeling on the anisotropic properties of soft sedimentary rock. Dissertation, Chang An University, China, 2017. (in Chinese)
44. Song I, Suh M (2014) Effects of foliation and microcracks on ultrasonic anisotropy in retrograde ultramafic and metamorphic rocks at shallow depths. *J Appl Geophys* 109:27–35
45. Su XQ, Nguyen S, Haghighat E, Pietruszczak S, Labrie D, Barnichon JD, Abdi H (2009) Characterizing the mechanical behaviour of the Tournemire argillite. In: Norris S, Bruno J, Van Geet M, Verhoef E (eds) *Radioactive Waste Confinement: Clays in Natural and Engineered Barriers*. Geological Society, London, p 443
46. Tan X, Konietzky H, Fruhwirt T, Dan DQ (2015) Brazilian tests on transversely isotropic rocks: laboratory testing and numerical simulations. *Rock Mech Rock Eng* 48:1341–1351
47. Tien YM, Kuo MC (2001) A failure criterion for transversely isotropic rocks. *Int J Rock Mech Min* 38(3):399–412
48. Wang SL, Yin XT, Tang H, Ge XR (2010) A new approach for analyzing circular tunnel in strain-softening rock masses. *Int J Rock Mech Min Sci* 47:170–178
49. Weibull GW (1951) A statistical distribution function of wide applicability. *J Appl Mech* 18:293–297
50. Wu SC, Xu XL (2016) A study of three intrinsic problems of the classic discrete element method using flat-joint model. *Rock Mech Rock Eng* 49(5):1813–1830
51. Xia L, Zeng Y (2018) Parametric study of smooth joint parameters on the mechanical behavior of transversely isotropic rocks and research on calibration method. *Comput Geotech* 98:1–7
52. Xie N, Zhu QZ, Xu LH, Shao JF (2011) A micromechanics-based elastoplastic damage model for quasi-brittle rocks. *Comput Geotech* 38:970–977
53. Xu GW, He C, Su A, Chen ZQ (2018) Experimental investigation of the anisotropic mechanical behavior of phyllite under triaxial compression. *Int J Rock Mech Min* 104:100–112
54. Xu GW, He C, Chen ZQ (2019) Mechanical behavior of transversely isotropic rocks with non-continuous planar fabrics under compression tests. *Comput Geotech* 115:103175
55. Xu DP, Feng XT, Chen DF, Zhang CQ, Fan QX (2017) Constitutive representation and damage degree index for the layered rock mass excavation response in underground openings. *Tunn Undergr Space Technol* 64:133–145
56. Yang SQ, Yin PF, Huang YH, Cheng JL (2019) Strength, deformability and X-ray micro-CT observations of transversely isotropic composite rock under different confining pressures. *Eng Fract Mech* 214:1–20
57. Zeng QD, Yao J, Shao JF (2018) Numerical study of hydraulic fracture propagation accounting for rock anisotropy. *J Pet Sci Eng* 160:422–432
58. Zhang XM (2010) Experimental study on anisotropic strength properties of sandstone. *Electron J Geotech Eng* 15:1325–1335
59. Zhou YY, Feng XT, Xu DP, Fan QX (2017) An enhanced equivalent continuum model for layered rock mass incorporating bedding structure and stress dependence. *Int J Rock Mech Min Sci* 97:75–98

Publisher's Note Springer Nature remains neutral with regard to jurisdictional claims in published maps and institutional affiliations.